Article

Strong Coupling between Biomineral Morphology and Sr/Ca of *Arctica islandica* (Bivalvia)—Implications for Shell Sr/Ca-Based Temperature Estimates

Cornélia Brosset [1,*], **Nils Höche** [1], **Kotaro Shirai** [2], **Kozue Nishida** [3], **Regina Mertz-Kraus** [1] **and Bernd R. Schöne** [1,*]

1   Institute of Geosciences, University of Mainz, Johann-Joachim-Becher-Weg 21, 55128 Mainz, Germany; nhoeche@uni-mainz.de (N.H.); mertzre@uni-mainz.de (R.M.-K.)
2   Atmosphere and Ocean Research Institute, The University of Tokyo, Chiba 277-8564, Japan; kshirai@aori.u-tokyo.ac.jp
3   Graduate School of Life and Environmental Sciences, University of Tsukuba, Tsukuba 305-8577, Japan; nishida.kozue.fw@u.tsukuba.ac.jp
*   Correspondence: cornelia.brosset@uni-mainz.de (C.B.); bernd.schoene@uni-mainz.de (B.R.S.)

Abstract: Bivalve shells serve as powerful high-resolution paleoclimate archives. However, the number of reliable temperature proxies is limited. It has remained particularly difficult to extract temperature signals from shell Sr/Ca, although Sr is routinely employed in other biogenic aragonites. In bivalves, Sr/Ca is linked to the prevailing microstructure and is sometimes affected by kinetics. Here, the hypothesis is tested that temperature can be reconstructed from shell Sr/Ca once microstructure and/or growth-rate-related bias has been mathematically eliminated. Therefore, the relationship between Sr/Ca and increment width, as well as biomineral unit size, has been studied in three different shell portions of field-grown *Arctica islandica* specimens. Subsequently, microstructure and/or growth-rate-related variation was removed from Sr/Ca data and residuals compared to temperature. As demonstrated, the hypothesis could not be verified. Even after detrending, Sr/Ca remained positively correlated to water temperature, which contradicts thermodynamic expectations and findings from inorganic aragonite. Any temperature signal potentially recorded by shell Sr/Ca is overprinted by other environmental forcings. Unless these variables are identified, it will remain impossible to infer temperature from Sr/Ca. Given the coupling with the biomineral unit size, a detailed characterization of the microstructure should remain an integral part of subsequent attempts to reconstruct temperature from Sr/Ca.

Keywords: shell microstructure; biomineral unit; bivalve sclerochronology; Sr/Ca; seasonal growth rate; temperature proxy

1. Introduction

Bivalve mollusks offer outstanding potential for paleoclimate research [1–7]. They are biogeographically widely distributed, occur abundantly and are sometimes excellently preserved in the fossil record. Based on shell growth pattern analysis, each sample taken from the shells can be accurately dated to the nearest calendar year [8,9], day [10–12] or tidal cycle [13–15], provided that the time of death or birth is known. While some species only live for several months or years, offering valuable insights into sub-seasonal environmental variability [16–19], others attain a lifespan of several hundred years [2,3,20–25]. The latter can be used to reconstruct decadal and century-scale climate dynamics [4,26–32], specifically if the growth increment series of many specimens with overlapping lifespans are crossdated to form stacked chronologies that cover centuries to millennia, and can provide well-replicated climate data [3,31,33,34].

Despite major advances in bivalve sclerochronology during the last decade [35], the quantitative reconstruction of environmental variables from shells, specifically ocean temperature, remains a challenging task owing to the very limited number of well-accepted proxies and the dual nature of many of those. For example, the stable oxygen isotope value, by far the most frequently used surrogate for temperature in bivalves and other biogenic archives, simultaneously records changes in temperature and the $\delta^{18}O$ signature of the ambient water [36,37]. Given that most bivalve species form their shells near oxygen isotopic equilibrium with the water [38–40], temperatures can be reliably estimated from $\delta^{18}O_{shell}$ as long as the $\delta^{18}O_{water}$ value is known or can be otherwise inferred, e.g., from salinity [41], which is strongly correlated to $\delta^{18}O_{water}$. The shell growth rate, another potential temperature proxy in shells, is likewise controlled by several environmental variables, i.e., temperature, food supply and food quality—e.g., [42–45]. Unless the influence of food conditions on the shell growth rate has been quantified, changes in increment width cannot provide precise temperature data. Amongst others, carbonate clumped isotopes overcome the duality dilemma of the aforementioned proxies [46–49] and can potentially occupy a prominent place in future bivalve sclerochronological studies. However, analytical refinement is still needed, namely a reduction in error, sample size, sample throughput, etc.

In many other biogenic carbonates, strontium (in aragonite) and magnesium (in calcite) can provide reliable temperature proxy data—e.g., [50,51]. However, in bivalves, the interpretation of these elements has remained notoriously difficult. In particular, the use of Sr in aragonitic shells as a proxy for temperature has been hotly debated, and many controversial findings have been reported on the relationship with temperature, ranging from negative to positive correlations to none at all—e.g., [52–59]. Some studies even reported a link between Sr and the shell growth rate [60], rather than temperature. There is a broad consensus, however, that the incorporation of Sr into shell aragonite is controlled by vital and kinetic effects. This is firstly indicated by much smaller distribution coefficients than in abiogenically precipitated aragonite [61]. Secondly, in most studies in which the expected negative correlation between Sr/Ca and temperature was found, the temperature sensitivity of shell Sr/Ca differed from thermodynamic expectations [62–66]. Another important, common observation is that the shell Sr content is tightly linked to the prevailing shell microstructure [55,67–69], with strong enrichment at the growth lines (reflecting periods of slow growth) and much lower values in the portions between adjacent growth lines (=growth increments, periods of fast growth). For example, in *Arctica islandica*, shell Sr/Ca values of more than 3 mmol/mol were measured in annual growth lines (consisting of irregular simple/spherulitic prismatic [ISP] microstructure; for an overview on abbreviations used in this paper, see Appendix A, Table A1), whereas those in the annual growth increments (homogenous [HOM] microstructure in the outer portion of the outer shell layer [oOSL]; crossed-acicular microstructure [CA] in the inner portion of the outer shell layer [iOSL]) fluctuated between 0.7 and 1.3 mmol/mol [56,70]. Values in contemporaneous shell portions of the oOSL were higher than those in the iOSL [70,71]. Similar differences were observed at a higher resolution within the annual increment of *Cerastoderma edule*. While 3.5 mmol/mol Sr/Ca was measured in circatidal growth lines (formed during low tide; ISP in iOSL), the circatidal increments (reflecting growth during high tide; nondenticular composite prismatic in iOSL) contained only 2.5 mmol/mol [68]. It is worth noting that, in artificially cultivated bivalves, the shell microstructure is often much more uniform than in field-grown specimens [72], and, in such bivalves, a statistically significant negative correlation between shell Sr/Ca and temperature has occasionally been reported [66].

Based on these findings, it is hypothesized here that temperature can be reconstructed from shell Sr/Ca data once the microstructure and/or growth-rate-related bias has been mathematically eliminated. To test this hypothesis, we have investigated the relationship between molar shell Sr/Ca values and morphological parameters (area, elongation) of the individual building blocks of the shell microstructure, i.e., individual biomineral units (BMUs), in three different shell portions of field-grown *A. islandica* with a specific

microstructure (oOSL: HOM, iOSL and hinge: CA). Furthermore, the coupling between Sr/Ca and the growth rate was studied. In a subsequent step, we have mathematically removed the microstructure and/or growth-rate-related variation from the shell Sr/Ca data and compared the residuals to seasonal water temperature changes. The focus was placed on BMU variations occurring during the main growing season, i.e., within annual increments and, thus, the same microstructure category. If it were possible to unlock the temperature information encoded in shell Sr/Ca, bivalve sclerochronology would make a major leap forward and boost paleoclimate research.

2. Materials and Methods

2.1. Sample Material and Preparation

To assess the link between Sr/Ca values, growth rate and microstructural properties (BUM area and elongation) of the shells at high resolution (weekly/monthly), three live-collected, juvenile specimens of *A. islandica* were studied (Table 1). The bivalves were obtained by dredging from 7 m water depth at Þistilfjördur, NE Iceland (66°11′ N, 015°21′ W), on 17 August 2006. After return to the coast, the bivalves were shucked, and the shells were rinsed with tap water. In the laboratory, the left valve of each specimen was mounted on an acrylic glass cube using WIKO Multi Power 3 plastic welder. Along the prospective cutting axis, the outer and inner shell surfaces were covered with a protective layer of WIKO 05 metal epoxy resin. Once the plastic welder and epoxy resin had cured, two approx. 2.5 mm-thick sections were cut from each valve along the axis of maximum growth (Figure 1a) using a Buehler IsoMet 1000 low-speed saw (operated at 200 rpm) equipped with a 0.4 thick diamond wafering blade (Buehler 15LC 11-4255). Subsequently, both sections were ground on glass plates using F800 and F1200 SiC suspensions and polished with 1 μm Al_2O_3 suspension on a Buehler MasterTex polishing cloth. After each preparation step, the shell sections were ultrasonically cleaned in tap water. One section of each specimen was then glued to a glass slide and used for in situ chemical analysis via laser ablation inductively coupled plasma mass spectrometry (LA-ICP-MS), whereas the mirroring section was attached to a one-inch sample holder with a carbon sticker for microstructure analysis via scanning electron microscopy (SEM).

Table 1. Overview of specimens of *Arctica islandica* used in present study along with number of chemical analyses and areas in which microstructural analyses were conducted. Bivalves were collected alive at Þistilfjördur, NE Iceland (66°10′ N, 015°21′ W) on 17 August 2006. SEM = scanning electron microscopy; LA = laser ablation.

Specimen ID	Ontogenic Age (yr)	# SEM Images		# LA Spots	
		Ventral Margin	Hinge	Ventral Margin	Hinge
ICE06-6.2-A201L	7	318	44	315	31
ICE06-6.2-A202L	6	353	21	351	21
ICE06-6.2-A203L	4	259	15	298	21
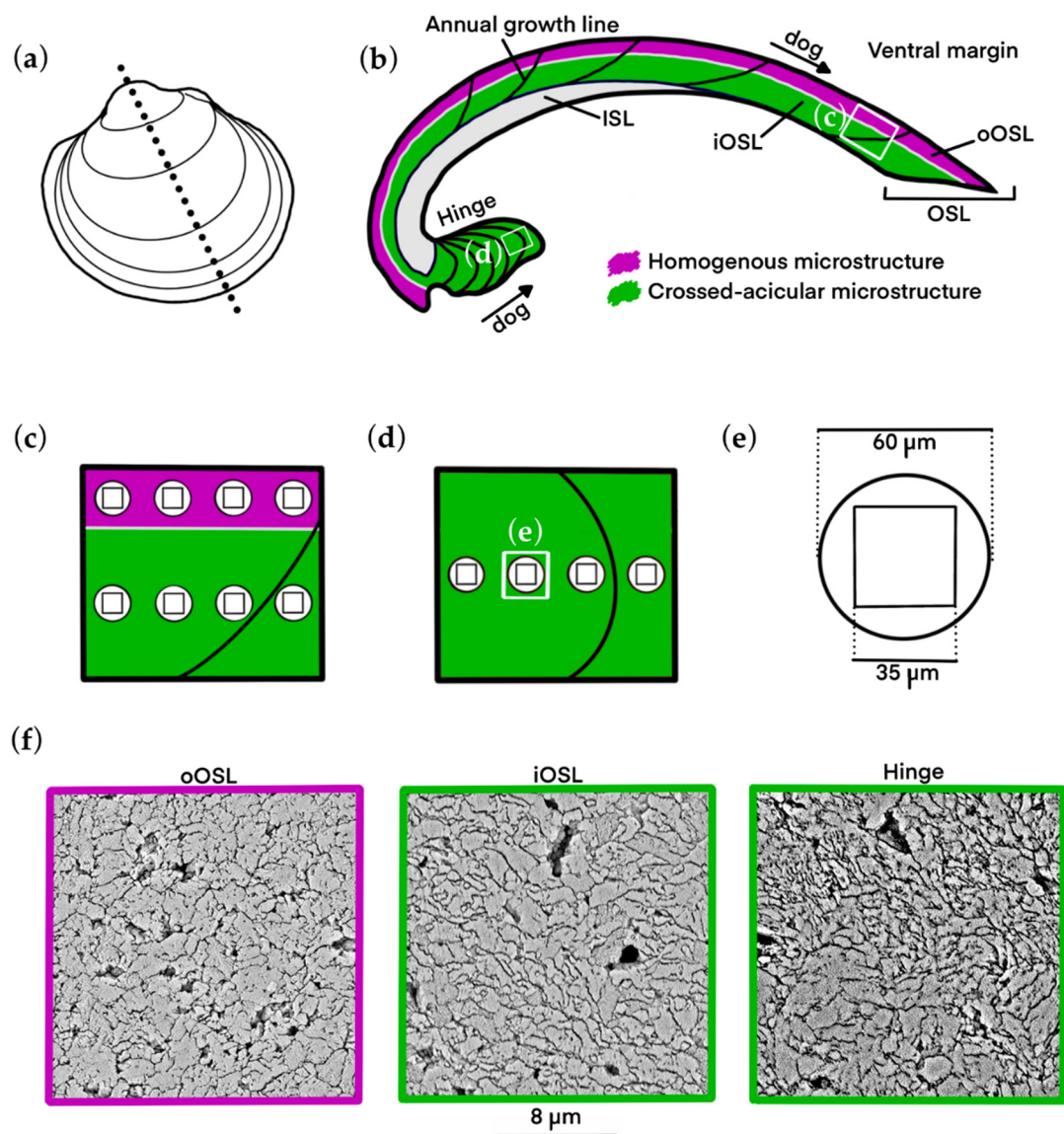
Figure 1. Overview of positions where element chemical and microstructural analyses were performed in shells of *Arctica islandica*. (**a**) Schematic representation of the left valve showing the cutting axis along (black dotted line). (**b**) Cross-sectioned shell slab showing different shell layers and dominant microstructures. The outer and inner shell layers (OSL, ISL) are separated by the myostracum. The OSL is further subdivided into an outer and inner portion (oOSL, iOSL). Homogenous microstructure (magenta) dominates the oOSL and crossed-acicular microstructure (green) prevails in the iOSL and hinge. The direction of growth (dog) of each shell portion is indicated by arrows. (**c**) An enlargement of panel (**b**) showing the sampling positions for microstructural and in situ chemical analyses in the ventral margin. (**d**) An enlargement of panel (**b**) showing the sampling positions for microstructural and in situ element chemical analyses in the hinge. (**e**) Schematic representation of a laser spot (diameter = 60 µm) for in situ chemical analysis and a SEM image (square of 35 µm). (**f**) Microstructure examples: HOM and CA in the ventral margin, and CA in the hinge. The scale underneath applies to all SEM images.

2.2. In-Situ Chemical Analysis (LA-ICP-MS)

The LA-ICP-MS system at the Institute of Geosciences, University of Mainz consisted of a 193 nm ArF Eximer laser (ESI NWR 193) coupled to an Agilent 7500ce quadrupole ICP-MS. The laser repetition rate was set to 10 Hz at an approximate energy density of 3 J/cm^2. For each sample, 15 s of background measurement time were followed by

30 s of ablation and 20 s of wash-out time. Measurements were performed in single spot mode (*n* = 1037) using a beam diameter of 60 μm. The distance between the spot centers was c. 90 μm. Laser tracks were positioned parallel to the main growth axis. To assess the relationship between shell Sr/Ca data and the BMU morphology of different microstructure categories (HOM, CA) that were deposited simultaneously in different shell portions, analyses were completed in the hinge and both sublayers of the outer shell layer (oOSL, iOSL; Figure 1b–e; see Table A1 for overview on abbreviations used in this paper). This way, three contemporaneous shell Sr/Ca chronologies were measured in each specimen.

Accuracy and precision of the analyses were monitored with USGS MACS-3, BCR-2G, JCp-1 and JCt-1 (for respective quality control data, see Table S1). NIST SRM 610 was used to calibrate the element concentrations of shells and the quality control materials using preferred values reported in the GeoReM database (available at http://georem. mpch-mainz.gwdg.de, ver. 30, last access: 1 March 2022; [73,74]). For data reduction, the time-resolved signals were processed using the software Glitter 4.4.1 [75]. Concentrations of strontium were determined from measured intensities of ^{88}Sr. Element-specific RSD% values, and average detection limit (computed as $3\sigma_{background}$ according to [76]) is listed in the Table S1. ^{43}Ca served as the internal standard for reference materials and shells. To convert the shell Sr concentration data to molar shell Sr/Ca ratios (mmol/mol), a constant ^{43}Ca concentration of 380,000 μg/g was assumed [77].

2.3. Microstructure Morphometry

The remaining section of each specimen was prepared for microstructure analysis via SEM according to the method reported by [78]. To identify individual BMUs under the SEM, ultrafine chemo-mechanical polishing was performed. For this purpose, the sections were polished for 10 min on a Buehler MetaServ 2000 rotational lap at 50 rpm with a Buehler MasterTex polishing cloth and Buehler MasterMet polishing suspension. This suspension has a grain size of 60 nm and an alkaline pH of ca. 10.1, allowing for removal of the inter-crystalline organics while minimizing crystalline abrasion of the section surface [78]. In order to directly compare microstructural properties with shell Sr/Ca values, SEM images (35 μm × 35 μm) used for the analysis of BMU area and elongation were taken along contemporaneous transects as the laser ablation spots (Figure 1b–e). The SEM images were taken with a Phenom Pro Desktop SEM (3rd generation) equipped with a CeB$_6$ electron source and backscatter electron detector at 7700× magnification and 10 keV. To prepare the images for morphometric studies, it was necessary to detect the individual BMUs in the SEM images. This process is called 'image segmentation' and was performed using the machine-learning-based image processing program Ilastik [79]. After some train-ing, and aside from manual quality screening of the resulting image segmentations, the software program was able to discern individual BMUs without further user interaction. Unsatisfactory results were excluded from further analysis and measurements were re-peated. BMU recognition was exclusively performed within annual increments to ensure that data only came from one microstructure category. Therefore, images crossing annual growth lines were discarded. In *A. islandica*, annual growth lines are composed of irregular simple/spherulitic prismatic (ISP) microstructure. It should be added that annual growth lines were also too narrow (barely more than c. 10 μm in width) to obtain a sufficient number of BMU data required for a statistically sound analysis. In each remaining SEM image (*n* = 1010), the BMU area and elongation (estimated by an ellipse-fit; measured as the ratio between the longest and shortest BMU axes) were automatically measured using the image processing library scikit-image [80] and the python script from [81]. As indicated by previous studies, most morphological variation occurs among the largest BMUs, and, in this size group, the relationship between the microstructural properties and temperature is largest [72]. Therefore, only the 15% largest BMUs of each SEM image were used in subsequent analyses.

2.4. Temporal Alignment and Re-Sampling of the Shell Sr/Ca and BMU Data

In order to compare the datasets with each other, it was firstly required to convert the distance axis (=sample track) to a time axis, i.e., to temporally align the chemical and microstructural data of the shells, considering variable seasonal shell growth rates. For this purpose, the shells were photographed (Canon EOS 600D DSLR) under a reflected light microscope (Leica Stemi 508) and the images were stitched together with the Microsoft Image Composite Editor. Then, the position (=center) of each sample relative to the last annual growth line was determined using the image processing software ImageJ. In conjunction with the cumulative version of the seasonal shell growth model of *A. islandica* for shallow surface waters (recently refined by [78], Figure 2b), it was then possible to assign a calendar date to the center of each LA spot and each SEM image.
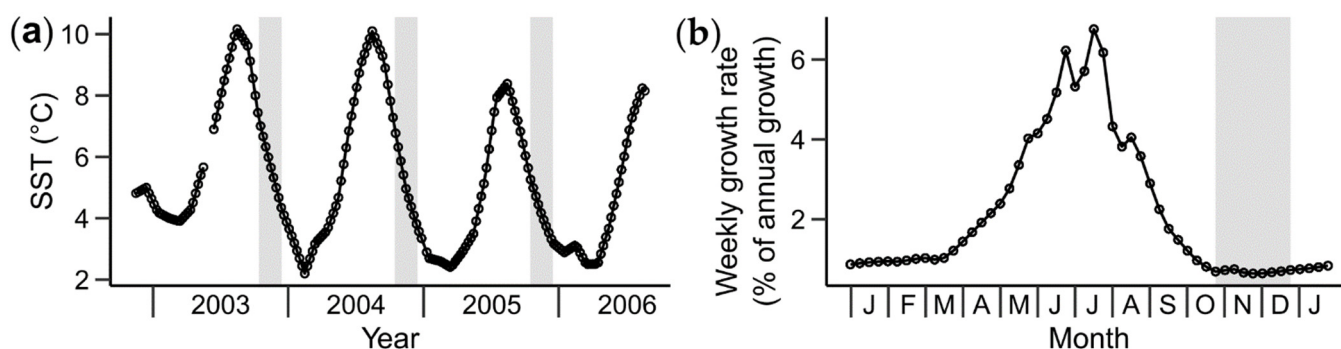
Figure 2. Water temperature and typical seasonal shell growth of *Arctica islandica*. (**a**) Weekly sea surface temperature data at Grímsey station [82] between December 2003 and August 2006. (**b**) Seasonal shell growth model (weekly resolution) of *Arctica islandica* in shallow waters based on [78]. Vertical gray bars denote annual growth lines.

Once the sample positions were temporally contextualized, it was necessary to compute a new set of chronologies that can directly be compared with both each other and instrumental sea surface temperature (SST). This mathematical conversion was needed because each of the original samples represented different amounts of time and the time intervals between the centers of the samples varied. To compute chronologies of consistent temporal resolution, the portions between the sample centers were linearly interpolated (i.e., temporally aligned data were connected with lines), and the generated curves were re-sampled at equidistant time intervals to obtain monthly and weekly resolved chronologies. Due to differences in absolute growth rate, the annual increment width was considerably smaller in the hinge than in contemporaneous portions of the ventral margin. Thus, the time-averaging of the samples was larger in the hinge than in the ventral margin. Based on the lowest temporal resolution of the original data, a monthly resampling was chosen for data obtained from the hinge, and a weekly resampling for those obtained from the ventral margin.

2.5. Regression Analysis and Detrending of Shell Sr/Ca Data

To assess the relationship between chemical properties and growth rate, Sr/Ca values were layer-specifically (oOSL, IosL) plotted against weekly increment width (absolute values deducted from the annual growth model for each annual increment). Linear regression curves were then computed for Sr/Ca_{oOSL} versus weekly increment width and Sr/Ca_{iOSL} versus weekly increment width (Table 2). To evaluate the relationship between chemical and microstructural properties of the shells, eight regression curves were computed for the following data pairs: (1) Sr/Ca_{vm} vs. BMU area, (2) Sr/Ca_{vm} vs. BMU elongation, (3) Sr/Ca_{oOSL} vs. BMU area, (4) Sr/Ca_{oOSL} vs. BMU elongation, (5) Sr/Ca_{iOSL} vs. BMU area, (6) Sr/Ca_{iOSL} vs. BMU elongation, (7) Sr/Ca_{hinge} vs. BMU area and (8) Sr/Ca_{hinge} vs. BMU elongation.

Table 2. Overview of the relationships (Pearson correlation; r = correlation coefficient; R^2 = coefficient of determination; *p* = probability) between the shell Sr/Ca data of *Artica islandica* and sea surface temperature (SST), biomineral unit (BMU) area and elongation and shell growth rate (weekly increment width). The relationships were examined for undetrended Sr/Ca data of the outer and inner portions of the outer shell layer (oOSL and iOSL, respectively), as well as both sublayers combined (referred to as vm = ventral margin). Regression models were computed for Sr/Ca values detrended (d) for growth rate (d_{GR}) and BMU size (d_{MS})-related effects for the iOSL, oOSL and vm. Magenta vm = homogenous microstructure; green vm = crossed-acicular microstructure. d_{GRMS} stands for double detrending.

| Variables		SST (°C)	BMU Area (μm²)	Weekly Increment Width (μm)	BMU Elongation
Sr/Ca	vm	$r = 0.15$ $p < 0.001$	$r = -0.56$ $R^2 = 0.31$ $p < 0.001$	$r = 0.13$ $R^2 = 0.02$ $p < 0.001$	$r = -0.03$ $p = 0.465$
	oOSL	$r = 0.10$ $R^2 = 0.01$ $p = 0.069$	$r = -0.39$ $R^2 = 0.15$ $p < 0.001$	$R^2 = 0.02$ $p < 0.005$	$r = 0.02$ $R^2 = 0$ $p = 0.735$
	iOSL	$r = 0.10$ $R^2 = 0.20$ $p < 0.001$	$r = -0.68$ $R^2 = 0.46$ $p < 0.001$	$R^2 = 0.26$ $p < 0.001$	$r = -0.44$ $R^2 = 0.19$ $p < 0.001$
	hinge	$r = -0.04$ $R^2 = 0.00$ $p = 0.823$	$r = -0.12$ $R^2 = 0.01$ $p = 0.560$		$r = 0.01$ $R < 0.01$ $p = 0.980$
d_{GR}Sr/Ca	vm	$r = 0.01$ $R^2 < 0.01$ $p = 0.908$			
	vm	$r = 0.40$ $R^2 = 0.16$ $p < 0.001$			
	oOSL	$r = 0.18$ $R^2 = 0.03$ $p < 0.001$	$r = -0.43$ $R^2 = 0.19$ $p < 0.001$		
	iOSL	$r = 0.27$ $R^2 = 0.07$ $p < 0.001$	$r = -0.58$ $R^2 = 0.33$ $p < 0.001$		
d_{MS}Sr/Ca	vm	$r = 0.22$ $R^2 = 0.05$ $p < 0.001$			
	vm	$r = 0.49$ $R^2 = 0.24$ $p < 0.001$			
	oOSL	$r = 0.20$ $R^2 = 0.04$ $p < 0.001$			
	iOSL	$r = 0.51$ $R^2 = 0.26$ $p < 0.001$			
d_{GRMS}Sr/Ca	iOSL	$r = 0.32$ $R^2 = 0.10$ $p < 0.001$			
	oOSL	$r = 0.29$ $R^2 = 0.08$ $p < 0.001$			

In a subsequent step, the possible influence of BMU area and/or shell growth rate was removed from shell Sr/Ca data measured in the ventral margin (note that the number of hinge data was insufficient for a respective mathematical conversion and that BMU elongation did not show consistent relationships with Sr/Ca). In practice, the correlation between Sr/Ca and BMU area, as well as between Sr/Ca and shell growth, was mathematically eliminated, and shell Sr/Ca thus detrended. This was accomplished in a similar way, as ontogenetic age trends are removed from annual increment widths of bivalves [83]. Detrended Sr/Ca data were computed by subtracting measured by predicted Sr/Ca values, where the predicted values are obtained from the regression curves (Sr/Ca vs. growth rate or BMU area, respectively). The resulting data provide a measure of how shell Sr/Ca values deviate from the regression curve. The following detrended shell Sr/Ca chronologies were computed: (1) $d_{GR}Sr/Ca_{oOSL}$, (2) $d_{GR}Sr/Ca_{iOSL}$, (3) $d_{GR}Sr/Ca_{vm}$, (4) $d_{MS}Sr/Ca_{oOSL}$, (5) $d_{MS}Sr/Ca_{iOSL}$, (6) $d_{MS}Sr/Ca_{vm}$, (7) $d_{GRMS}Sr/Ca_{oOSL}$, (8) $d_{GRMS}Sr/Ca_{iOSL}$ and (9) $d_{GRMS}Sr/Ca_{vm}$, where the prefix 'd' stands for 'detrended' and the following subscript denotes how the Sr/Ca data (of the respective shell portions: oOSL, iOSL and vm) were detrended, i.e., by growth rate (GR), microstructure (MS) or a combination of both (GRMS). Detrended and non-detrended Sr/Ca data, as well as BMU morphology data of the two transects of the ventral margin, oOSL and iOSL, were then compared to each other using non-parametric Mann–Whitney U two-sample rank-sum tests. To assess possible links between SST and shell Sr/Ca data before and after detrending, Pearson correlations and corresponding levels of significance were calculated. SST data were obtained from Grímsey station (Figure 2a; [82]).

3. Results

### 3.1. Shell Strontium-to-Calcium Ratios and BMU Morphology

Temporally aligned, weekly resolved shell Sr/Ca chronologies were, at large, highly synchronous among the three studied specimens (Figure 3a). In both shell layers of the ventral margin, Sr/Ca_{vm} values gradually increased during the year, reached a maximum in summer (August) and declined toward the following annual growth line. Differences between the Sr/Ca curves of the two sublayers of the outer shell layer were observed during the beginning of the growing season. In the iOSL, the seasonal Sr/Ca minimum was typically attained shortly after the annual growth line (=November), i.e., during the beginning of the growing season (0.70 mmol/mol). However, in the oOSL, Sr/Ca values first increased stronger than in the iOSL, reached a local maximum in February and then declined again to attain the seasonal Sr/Ca minimum c. half-way between adjacent annual growth lines in the oOSL (1.08 mmol/mol; c. June/July) (Figure 3a). Sr/Ca_{vm} ratios were generally higher in the oOSL (1.55 ± 0.14 mmol/mol; average $\pm$ 1 standard deviation) than in the iOSL (1.11 ± 0.18 mmol/mol). In the iOSL, Sr/Ca attained highest values of 1.59 mmol/mol, whereas those of the oOSL reached 2.14 mmol/mol. Note that samples covering the annual growth lines exceeded the aforementioned values, on average, by 0.25 mmol/mol (Table S2). As explained in the preceding section, data from annual growth lines were excluded from the analysis.

As shown in Figure 3b, the average Sr/Ca_{vm} data differed significantly between the two sublayers of the outer shell layer (Mann–Whitney U, $p < 0.001$). Note that the two sublayers also differed by their shell microstructure. The oOSL consisted of HOM and the iOSL of CA microstructures. In contrast, contemporaneous shell portions of the hinge and ventral margin belonging to the same microstructure category (i.e., CA) contained statistically indistinguishable (Mann–Whitney U, $p = 0.299$) concentrations of Sr (Figure 3b). On average, the Sr/Ca values of the hinge (1.25 mmol/mol) were only 0.14 mmol/mol higher than those of the iOSL. However, Sr/Ca data of the hinge were statistically significantly (on average, 0.30 mmol/mol) lower than those of the oOSL (Mann–Whitney U, $p < 0.001$).
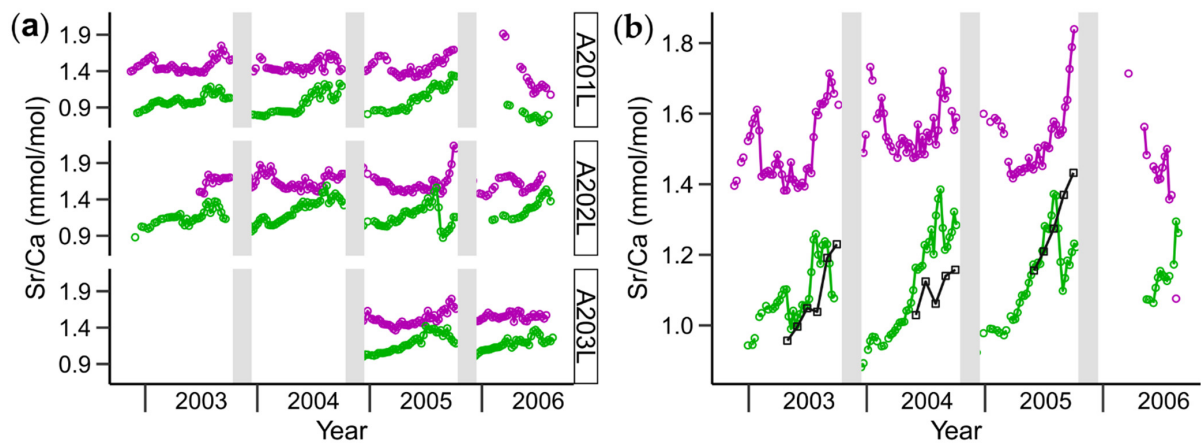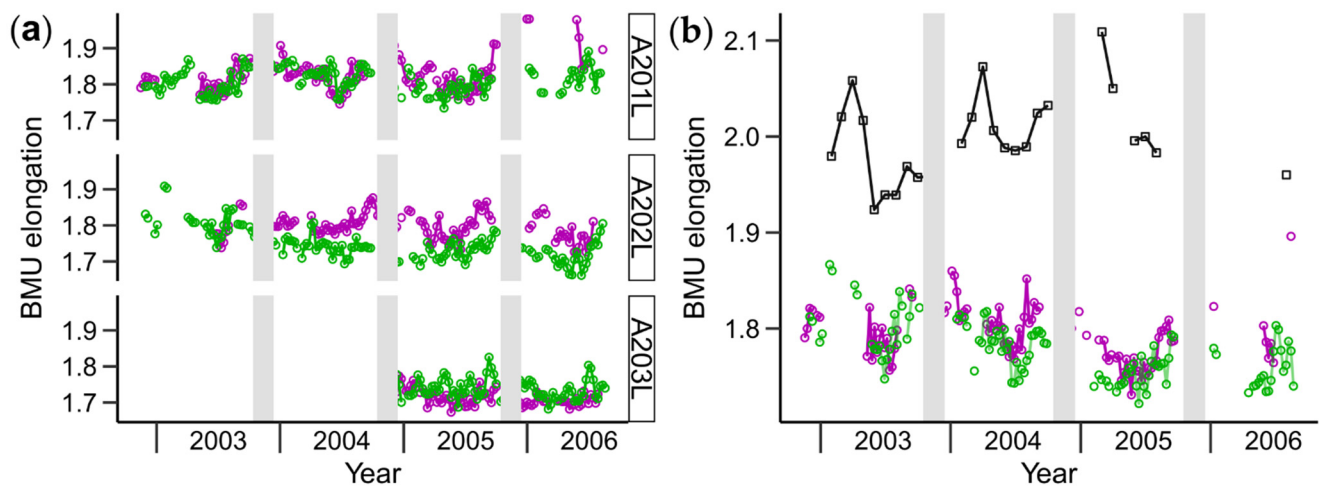
Figure 3. Shell Sr/Ca chronologies of the three studied specimens (A201L, A202L and A203L) of *Arctica islandica*. Magenta open circles = data from the outer portion of the outer shell layer (oOSL; homogeneous microstructure, HOM) of the ventral margin; green open circles = data from the inner portion of the outer shell layer (iOSL; crossed-acicular microstructure, CA) of the ventral margin; black open squares = data from the hinge (CA). Vertical gray bars denote annual growth lines. (**a**) Sr/Ca chronologies of each specimen and sublayer of the outer shell layer (oOSL, iOSL). (**b**) Average Sr/Ca chronologies computed from curves depicted in (**a**). Data from the ventral margin are weekly resolved. Monthly Sr/Ca data of the hinge (data from all studied specimens combined) are shown for comparison.

Aside from differences in their element chemistry and overall microstructure, the two sublayers of the outer shell layer revealed a statistically significant difference (Mann–Whitney U, $p < 0.001$) in the size of the biomineral units (BMUs) composing the CA and HOM microstructures (Figure 4). The BMUs of the iOSL (CA) were generally larger than those of the oOSL (HOM), with average areas of 0.98 ± 0.19 μm^2 and 0.85 ± 0.17 μm^2, respectively. While the Sr/Ca$_{vm}$ values were similar for all CA microstructures, irrespective of the shell portion (Sr/Ca$_{hinge}$ and Sr/Ca$_{iOSL}$), the CA BMUs were significantly larger (range between 0.94 μm^2 and 1.48 μm^2) in the hinge than in the ventral margin (c. 0.85 μm^2; Figure 4; Mann–Whitney U, $p < 0.001$).
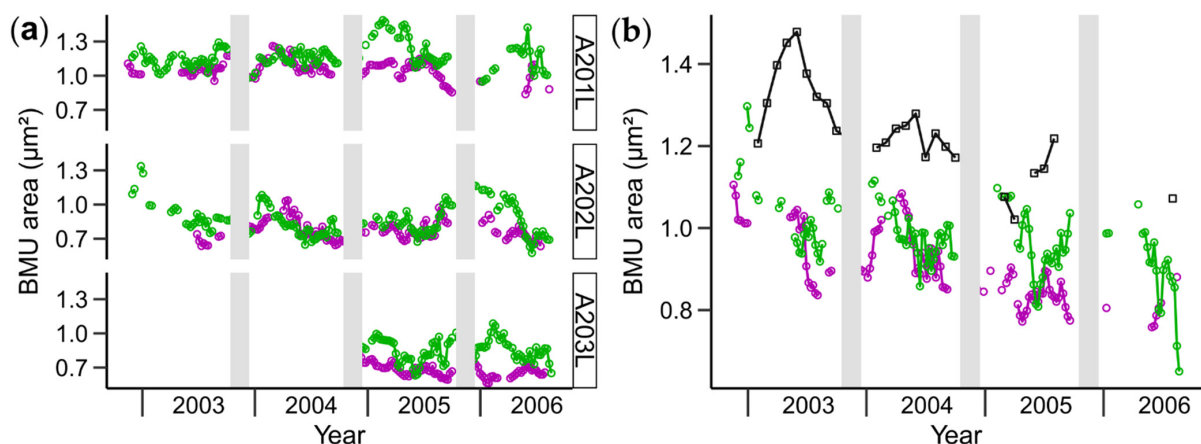
Figure 4. Average biomineral unit (BMU) area chronologies of the three studied shells (A201L, A202L and A203L) of *Arctica islandica*. Acronyms and color coding as in caption of Figure 3. Note, magenta = homogenous microstructure (oOSL); green = crossed-acicular microstructure (iOSL). Vertical gray bars denote annual growth lines. (**a**) BMU area chronologies of each specimen and sublayer of the outer shell layer (oOSL, iOSL). (**b**) Average BMU area chronologies computed from the curves depicted in (**a**). Data from the ventral margin are weekly resolved. Monthly Sr/Ca data of the hinge (data from all studied specimens combined) are shown for comparison.

The elongation of BMUs, in contrast, did not strongly differ between the specimens or shell portions (Figure 5). On average, the elongation of the CA BMUs of the iOSL was only 0.02 lower than the elongation of the HOM BMUs of the oOSL (average = 1.77 ± 0.05 and 1.79 ± 0.06, respectively). Moreover, the CA BMUs of the hinge were, on average, more elongated than those of the ventral margin. With an average of 1.99 ± 0.06, the elongation of the BMUs in the hinge differed significantly from those of the ventral margin (Mann–Whitney *U*, $p < 0.001$).


Figure 5. Average biomineral unit (BMU) elongation chronologies of the three studied shells (A201L, A202L and A203L) of *Arctica islandica*. Acronyms and color coding as in caption of Figure 3. Note, magenta = homogenous microstructure (oOSL); green = crossed-acicular microstructure (iOSL). Vertical gray bars = annual growth lines. (**a**) BMU elongation chronologies of each specimen and sublayer of the outer shell layer (oOSL, iOSL). (**b**) Average BMU elongation chronologies computed from the curves depicted in (**a**). Data from the ventral margin are weekly resolved. Monthly Sr/Ca data of the hinge (data from all studied specimens combined) are shown for comparison.

3.2. Relationships between Shell Sr/Ca, Growth Rate and BMU Morphology

Regression models for shell Sr/Ca and the growth rate, BMU area and BMU elongation are depicted in Figure 6. The mathematical relationship between shell Sr/Ca data and the growth rate was best described with non-linear regression models (Figure 6a and Table 2). In the iOSL, Sr/Ca values (Sr/Ca_{iOSL}) increased with the growth rate, but the opposite occurred in the oOSL. The strongest changes in Sr/Ca_{oOSL} and Sr/Ca_{iOSL} were observed during slow growth. If Sr/Ca data from both shell layers were combined (Sr/Ca_{vm}) in a single linear regression model, a weak positive linear correlation was found (r = 0.13, $p < 0.001$; Figure 6a and Table 2).

Sr/Ca values were negatively coupled with the BMU area (Figure 6b). If data pairs from the ventral margin (oOSL, iOSL) were combined in a regression model, the Pearson r equaled −0.56 ($R^2 = 0.32$; $p < 0.001$; Table 2). However, the strength and significance of this correlation varied within the different shell portions. The strongest relationship occurred in the iOSL (r = −0.68, $p < 0.001$), and the weakest in the hinge (r = −0.12, $p = 0.47$; Table 2). A moderately strong, though significant link between Sr/Ca and BMU area was observed in the oOSL (r = −0.39, $p < 0.001$; Figure 6b and Table 2). Shell portions consisting of the CA microstructure showed a larger variation in BMU area and contained less Sr than shell portions made of HOM. Much less covariation was observed between Sr/Ca and BMU elongation, and only in the iOSL were both parameters significantly coupled with each other, though not particularly strongly (r = −0.44, $p < 0.001$; Figure 6c and Table 2).
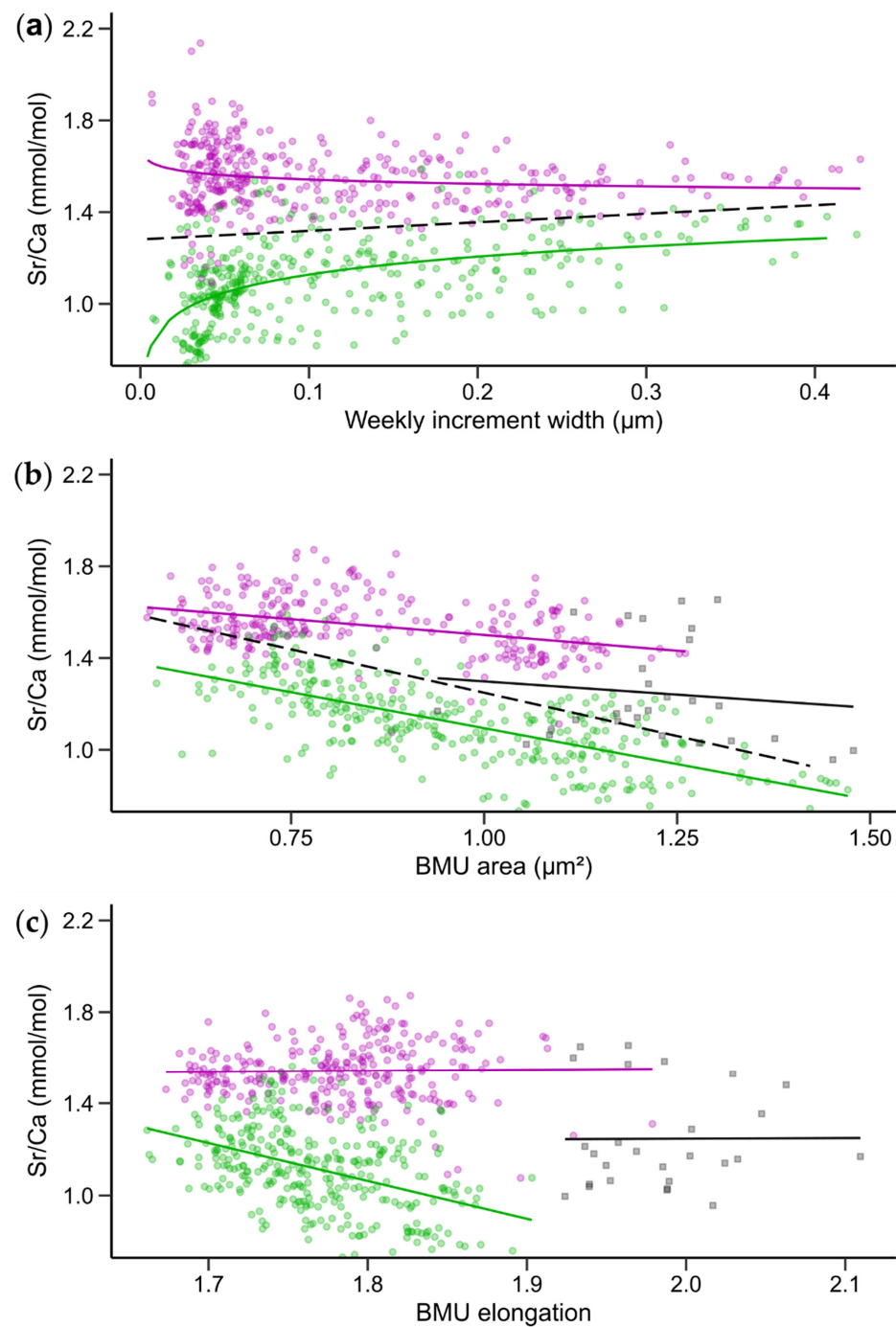
Figure 6. Relationships between Sr/Ca data and microstructural properties of *Arctica islandica* shells. Acronyms and color coding as in caption of Figure 3. BMU = biomineral unit. Note, magenta = homogenous microstructure (oOSL); green = crossed-acicular microstructure (iOSL); black = hinge. Green and purple data are weekly resolved, black data monthly. Regression curves are depicted in same color as data of respective shell portion. Black dashed lines represent linear regression model of entire outer shell layer (oOSL + iOSL) dataset. (**a**) In the inner portion of the outer shell layer (iOSL, magenta), shell Sr/Ca is weakly negatively linked to increment width, whereas a stronger and positive correlation exists in the outer sublayer of outer shell layer (oOSL, green). Note that non-linear models provided a better fit than linear models. When data from both OSL sublayers (oOSL, iOSL) are combined, a weak positive correlation is found with shell growth rate. (**b**) Shell Sr/Ca is negatively correlated to BMU area. (**c**) In the oOSL and hinge, shell Sr/Ca is weekly positively coupled to BMU elongation, but a stronger and negative correlation exists in the iOSL.

3.3. Growth Rate and BMU Area-Detrended Shell Sr/Ca Ratios

Based on the regression models depicted in Figure 6, the correlation with growth rate and/or BMU area was mathematically removed from the shell Sr/Ca data (Table 2). The resulting chronologies are depicted in Figure 7a–d. If the correlation with growth rate was shell-layer-specifically eliminated from the Sr/Ca data using the non-linear models for the iOSL and oOSL (Figure 6a), the resulting $d_{GR}Sr/Ca_{iOSL}$ and $d_{GR}Sr/Ca_{oOSL}$ chronologies (Figure 7a) were plotted much closer together than the non-detrended series depicted in Figure 3 and were statistically indistinguishable (Mann–Whitney U, $p = 0.808$). The new time-series also conserved most of the seasonal range of the original Sr/Ca_{oOSL} and Sr/Ca_{iOSL} data (Figure 3). However, if detrending was accomplished based on the regression model that combined Sr/Ca and growth rate data from both sublayers (Figure 6a), the new $d_{GR}Sr/Ca_{vm}$ time-series differed significantly from each other (Mann–Whitney U, $p < 0.001$) (Figure 7b) and were nearly identical to the non-detrended Sr/Ca_{vm} chronologies (Figure 3).
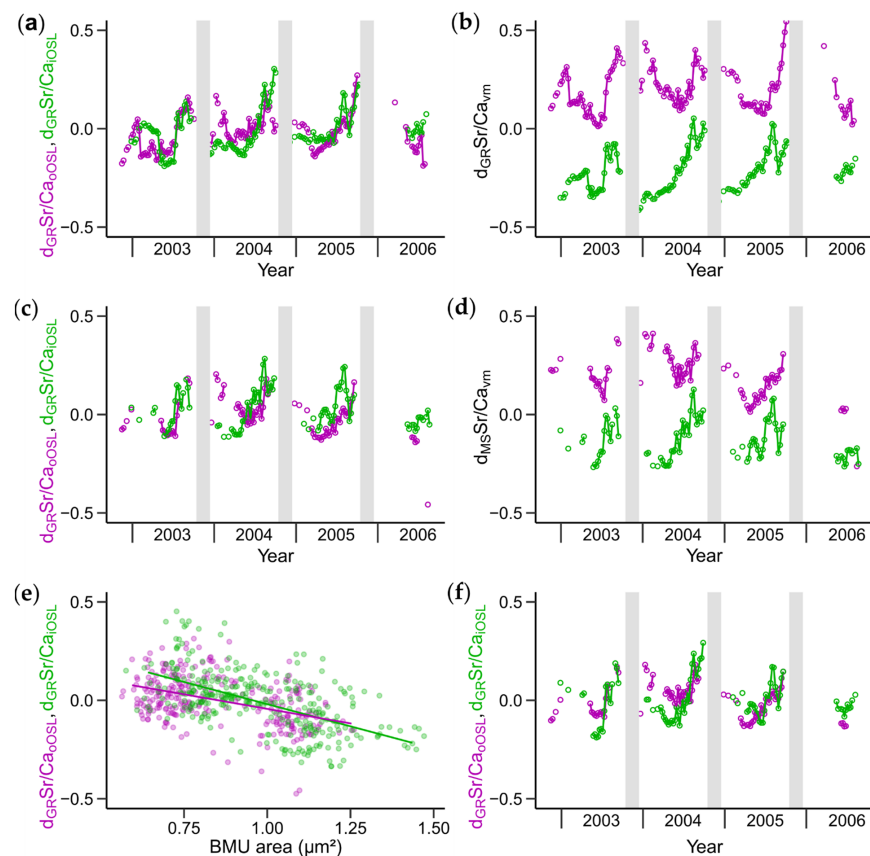
Figure 7. Detrended shell Sr/Ca chronologies of the outer and inner sublayers of the outer shell layer (oOSL, iOSL, respectively) of the ventral margin (vm) of *Arctica islandica*. Data represent averages of three specimens. Acronyms and color coding as in caption of Figure 3. (**a,b**) Growth rate (GR)-detrended Sr/Ca data. (**a**) Shell-sublayer-specific detrending based on non-linear models for oOSL and iOSL depicted in Figure 6a (magenta = $d_{GR}Sr/Ca_{oOSL}$; green = $d_{GR}Sr/Ca_{iOSL}$). (**b**) Detrending based on a regression model in which data from oOSL and iOSL (="vm") were combined (Figure 6a) (magenta = $d_{GR}Sr/Ca_{vm}$ of oOSL; green = $d_{GR}Sr/Ca_{vm}$ of iOSL). (**c,d**) BMU area (MS)-detrended Sr/Ca data. (**c**) Shell-sublayer-specific detrending based on linear models for oOSL and iOSL depicted in Figure 6b (magenta = $d_{MS}Sr/Ca_{oOSL}$; green = $d_{MS}Sr/Ca_{iOSL}$). (**d**) Detrending based on a regression model in which data from oOSL and iOSL (="vm") were combined (Figure 6a) (magenta = $d_{MS}Sr/Ca_{vm}$ of oOSL; green = $d_{MS}Sr/Ca_{vm}$ of iOSL). (**e**) Crossplot of growth-rate-detrended Sr/Ca (sublayer-specific detrending as in (**a**)) vs. BMU area. (**f**) Double detrended Sr/Ca chronologies based on linear models depicted in E (magenta = $_{GRMS}Sr/Ca_{oOSL}$; green = $_{GRMS}Sr/Ca_{iOSL}$).

The layer-specific detrending by the microstructure (here: BMU area) based on the regression models shown in Figure 6b also produced Sr/Ca chronologies ($d_{MS}Sr/Ca_{iOSL}$ and $d_{MS}Sr/Ca_{oOSL}$) that showed a stronger synchronicity with each other than the original curves (Figure 3), and their distributions were statistically indistinguishable (Mann–Whitney U, $p = 0.741$). However, the amplitudes were attenuated compared to the growth-rate-detrended (Figure 7a) and non-detrended Sr/Ca chronologies (Figure 3). As in the case of the growth-rate detrending, the Sr/Ca chronologies of the oOSL and iOSL were still strongly offset from each other if detrending was carried out based on the regression model that combined Sr/Ca and BMU size data from both sublayers of the OSL (Figure 7d). The $d_{MS}Sr/Ca_{vm}$ time-series were statistically different from each other (Figure 7d; Mann–Whitney U, $p < 0.001$) and revealed similar seasonal ranges to the Sr/Ca$_{vm}$ series (Figure 3).

A double detrending likewise resulted in strongly coherent Sr/Ca chronologies of the oOSL and iOSL (Figure 7f). For this purpose, the layer-specific growth-rate-detrended Sr/Ca data ($d_{GR}Sr/Ca_{iOSL}$ and $d_{GR}Sr/Ca_{oOSL}$) were plotted against the BMU area (Figure 7e). The linear regression curves were then used to further detrend the data, resulting in double-detrended Sr/Ca values. The $d_{GRMS}Sr/Ca_{iOSL}$ and $d_{GRMS}Sr/Ca_{oOSL}$ chronologies showed no statistical difference (Mann–Whitney U, $p = 0.847$), and, when plotted against time (Figure 7f), the seasonal variations had lower amplitudes than the undetrended Sr/Ca series (Figure 3).

3.4. Relationships between Sr/Ca Ratios and Water Temperature

Sr/Ca data of the ventral margin were weakly positively correlated to SST ($r = 0.15$; $p < 0.001$; Table 2). A slightly stronger link existed when layer-specific regression analyses were conducted (Figure 8a). In fact, Sr/Ca$_{iOSL}$ was the only profile that was significantly coupled to SST ($r = 0.45$, $p < 0.001$), whereas Sr/Ca$_{oOSL}$ was not ($r = 0.10$, $p = 0.07$; Table 2). Sr/Ca values of the hinge revealed no correlation with SST ($r = -0.04$, $p = 0.823$; Table 2).

While the growth-rate-detrended Sr/Ca data showed only extremely weak though statistically significant positive correlations with SST ($r = 0.18$ to 0.27, $p < 0.001$; Figure 8a,b and Table 2), the BMU-area-detrended Sr/Ca data of the iOSL data were more strongly tied to SST ($r = 0.51$, $p < 0.001$; Table 2). However, BMU-area-detrended Sr/Ca values of oOSL were only very weakly correlated to SST ($r = 0.20$, $p < 0.001$; Table 2). Double detrending resulted in weak correlations between Sr/Ca and SST in both OSL sublayers ($r = 0.30$, $p < 0.001$; Table 2).
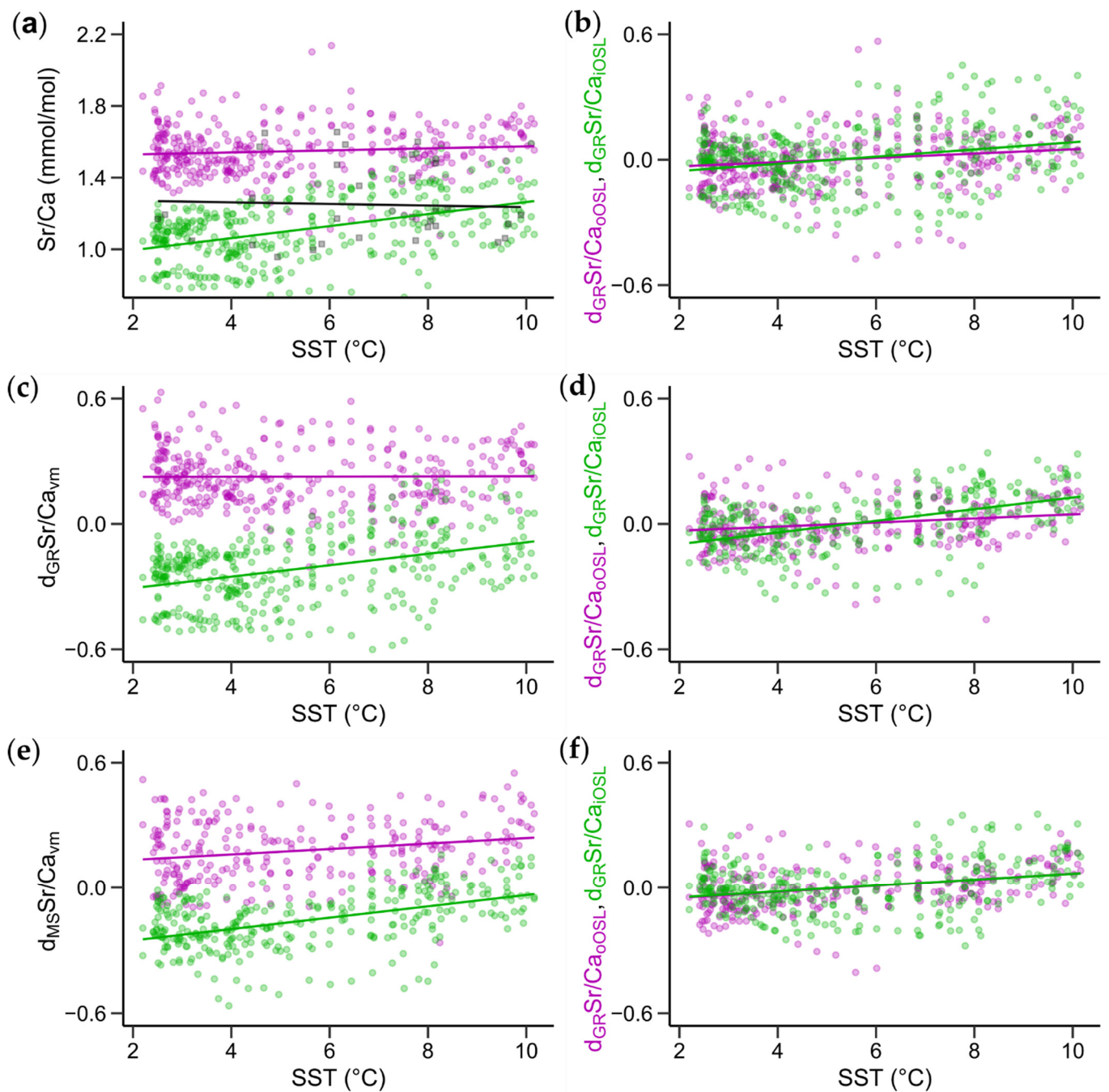
Figure 8. Relationships between shell Sr/Ca data of *Arctica islandica* and SST. Acronyms and color coding as in caption of Figure 3. (**a**) Undetrended Sr/Ca data; (**b**–**f**) detrended Sr/Ca data. (**a**) Shell Sr/Ca of the oOSL and iOSL are weakly positively correlated to sea surface temperature, and those from the hinge are not. (**b**,**c**) Growth rate (GR)-detrended Sr/Ca data. (**b**) Sublayer-specific detrending, (**c**) detrending based on all ventral margin data. (**d**,**e**) BMU area (MS)-detrended Sr/Ca data. (**d**) Sublayer-specific detrending, (**e**) detrending based on all ventral margin data. (**f**) Double-detrended Sr/Ca chronologies (growth rate + BMU area detrending, layer-specific as in (**a**,**c**)).

4. Discussion

Based on the findings presented here, the hypothesis examined in this study needs to be rejected. It does not seem to be possible to reconstruct water temperature from intra-annual shell Sr/Ca values of *A. islandica*, even if the growth rate and/or microstructure-related bias was mathematically removed from the data. Shell Sr/Ca values were weakly

and non-linearly linked to the shell growth rate and more strongly, linearly and likewise statistically significantly coupled with both the biomineral unit size and water temperature (Figures 6 and 8a). However, contrary to thermodynamic expectations for aragonite and results from inorganically precipitated aragonite [61,84], the seasonal shell Sr/Ca values were positively correlated to temperature (r = 0.15; Figure 8a), and remained so even after detrending by the growth rate and/or BMU area (r = 0.01 to 0.49; Figure 8b,d,f). Furthermore, the strong synchronicity among Sr/Ca chronologies of contemporaneous specimens suggests that other, unknown, environmental parameters exerted a strong control over the incorporation of strontium relative to calcium into the shell. Such a covariation would not be expected if the shell Sr content was largely governed by (individual) physiological processes.

4.1. Temperature Control of Shell Sr/Ca?

The development of environmental proxies in bivalve shells and other biogenic hard parts is typically based on empirical observations and supported by thermodynamic considerations or results from synthetically precipitated minerals. A strong running similarity of chemical or structural time-series among different contemporaneous specimens suggests a common response to an extrinsic forcing and represents a major prerequisite to establish an environmental proxy. For example, if shell growth rates change coherently among several contemporaneous specimens from the same habitat, it is highly likely that growth was controlled by environmental factors; in the case of bivalves, by a combination of temperature, food supply and food quality [42–45]. Likewise, a running similarity of element chemical profiles in shells of several coeval specimens—as observed in the present study for Sr/Ca—is typically considered as an indicator of environmental controls [77]. However, the specific environmental variables causing such common signals often remain enigmatic (e.g., Ba/Ca: [85]; various element/Ca ratios: [77]).

It can be tempting to infer causality from synchronicity and a statistically significant correlation between a given environmental variable, e.g., water temperature, and a chemical property, e.g., shell Sr/Ca, specifically if a relationship between these variables has previously been identified in synthetic $CaCO_3$ [61,84]. However, to substantiate a causal relationship between shell Sr/Ca and temperature, at least the sign of the regression curve needs to be identical to that observed in abiogenic precipitates, and, ideally, the intercept and the steepness of the regression slope should be similar as well. Since the Sr content of synthetic aragonite decreases with rising temperature [61,86], the observed positive correlation between the seasonal shell Sr/Ca of *A. islandica* and water temperature most likely does not reflect a causal relationship. The same applies to similar observations made in ocean quahogs in previous studies [87,88], as well as other species with aragonitic skeletons—e.g., [89].In most studies in which the thermodynamically expected negative correlation between the two variables could be verified [66,68], the temperature sensitivity of −0.02 mmol/mol/°C remained well below that observed in synthetic aragonite (−0.04 mmol/mol/°C, [61]; see [62–64]), suggesting that strong vital effects were at work. This view is further supported by consistently low concentrations of Sr in bivalve shells [57,58,90,91]. For example, in the studied specimens, shell Sr/Ca ratios remained, on average, almost eight to nine times below values expected for equilibrium fractionation at the same temperature range (2 to 10 °C: 1.34 ± 0.11 mmol/mol as opposed to c. 11 to 12 mmol/mol using Equation (8) of [61]; see further details in next section).

Theoretically, it appears possible that seawater Sr/Ca values varied on seasonal timescales—e.g., due to riverine influx [92]—and overprinted temperature signals potentially encoded in shell Sr/Ca. In that case, the studied shells would have predominantly recorded changes in seawater Sr/Ca. However, the study region was not affected by major rivers, and highly resolved Sr/Ca_water time-series are currently not available to evaluate the temporal variability of the water chemistry where the shells grew. Our own unpublished data indicate that Sr/Ca_water near the sample locality can spatially vary between 8.09 and 8.17 mmol/mol in surface water (66°11′58.68″ N, 015°23′32.76″ W and 66°11′23.46″ N,

015°20′34.02′′ W, respectively, 21 August 2012), and 8.12 and 8.13 mmol/mol in bottom water (ca. 10 to 20 m water depth; localities and date as before). If these changes remained unconsidered, temperature estimates would be off by 5 to 40 °C considering the weak temperature sensitivity of −0.02 mmol/mol/°C. Near Reykjavík (64°07′52.32′′ N, 021°57′38.35′′ W), the surface water Sr/Ca varied between 9.49 mmol/mol on 19 Apr 2012 and 8.02 mmol/mol on 21 May 2012. Certainly, more data are required to test the hypothesis of shells predominantly recording changes in water chemistry rather than temperature.

It remains unclear why annually averaged Sr/Ca values of old-grown *A. islandica* specimens from Iceland were moderately strongly and significantly negatively linked to water temperature [56], whereas intra-annual Sr/Ca values of conspecific specimens from the same locality (present study), other sites [87,88] or those grown in the laboratory [59], were not. Was [56] deceived by a spurious correlation, or were the shell Sr/Ca values of their study less strongly biased by other, unknown extrinsic factors than in the shells studied here, so that the actual negative relationship emerged? Or is the main reason for the significant negative correlation that Sr/Ca data from the annual growth lines were included in their analysis? As the calculations demonstrated in [56], annual growth lines may have formed near or even in chemical equilibrium with the ambient water. A possible reason for that is that, during growth line formation, the food supply was strongly reduced and thus so was the production of energy. Energy would be needed to biologically control the incorporation of Sr and other trace impurities into the shell (e.g., by actively pumping Sr^{2+} ions away from the site of biomineralization or producing organic macromolecules that can scavenge Sr^{2+} so that it cannot be incorporated into the shell). The remaining energy sufficed to form biominerals (ISP), but not to precipitate chemically 'pure' shell material. Elevated Sr/Ca values of the growth lines may have strongly contributed to the annual Sr/Ca average, resulting in an inverse relationship between annual Sr/Ca with SST. With an increasing ontogenetic age, annual growth lines become gradually broader and represent an increasingly larger proportion of annual increments. Hence, the contribution of growth line Sr/Ca values to the annual average gradually increases through its lifetime [56]. Accordingly, annual Sr/Ca values of ontogenetically older shell portions should be increasingly strongly negatively correlated to SST. These hypotheses should be tested in subsequent studies.

4.2. Relationship between Sr/Ca and Shell Microstructure

In the studied shells of *A. islandica*, the Sr concentration was distinctly inversely correlated to the BMU size, i.e., Sr/Ca values gradually decreased with an increasing BMU area. However, the regression slopes and, more importantly, the intercepts of the regression lines with the *y*-axis differed between the studied shell portions (Figure 6b). For that reason, it was not possible to effectively reduce the statistical difference between Sr/Ca_{oOSL} and Sr/Ca_{iOSL} chronologies based on a regression model in which data from both OSL sublayers were combined (Figures 6b and 7d). The differences in the regression lines suggest that Sr/Ca is not directly coupled to BMU size, but to other properties that covary with BMU area and/or Sr/Ca. This assumption is supported by the following observations: (i) the oOSL contained more Sr than the iOSL (which agrees with previous observations [70,71,93]) although the BMU size ranges were nearly the same in both OSL sublayers; (ii) based on the negative correlation between Sr/Ca and the BMU size, the lowest Sr concentration should be measured in the annual growth lines (which were not further analyzed in this study) because they contain the largest BMUs (ISP) of the entire shell [94–97]. However, the opposite is the case in *A. islandica* and other hitherto studied bivalves. The highest Sr concentrations are typically found in annual growth lines (Table S2, [68,70,71,98]); (iii) Sr/Ca values of the hinge show a different linear relationship with the BMU size than the Sr/Ca of the iOSL, despite consisting of the same microstructure type, i.e., CA (Figures 1b–f and 6b).

To identify variables that could have caused the apparent relationship between the BMU size and Sr/Ca values, the mechanism of Sr incorporation into the shells needs to

be considered. Due to similar ionic radii and charge, Sr^{2+} (132 pm) can substitute for Ca^{2+} (114 pm) in the crystal lattice of aragonite [99–101]. As experimentally demonstrated in inorganically precipitated aragonite, the Sr concentration decreases with an increasing temperature [84]. Inorganic aragonite precipitated at 15 °C contained 1.25 times as much Sr as present in the calcifying fluid, whereas, at 25 °C, this value—also known as the Doerner–Hoskins exchange coefficient—decreased to 1.16 [61]. Using the exchange equation provided by [61] (Equation (8)), and taking Sr/Ca values of the habitat of the studied *A. islandica* specimens into account (i.e., 8.5 to 8.8 mmol/mol cf. [102]), the shell Sr/Ca should vary between 11.05 and 12.24 mmol/mol for the observed temperature range of 2 to 10 °C (Figure 2a), provided the shells formed in chemical equilibrium with the ambient water (or biomineralization fluid). However, the measured shell Sr/Ca values (Figure 3) remained far below that figure, which agrees with many previous findings [57,58,90,91], suggesting that the incorporation of Sr into the shell is under strong biological control. This ensures, for example, that the optimal mechanical properties of the shell are maintained, which secures the survival of the bivalve (predator resistance). Increased amounts of trace impurities can increase the hardness of the $CaCO_3$ [103] at the expense of elasticity, i.e., a harder shell is more vulnerable to fractures. Given the inverse relationship between the shell Sr content and temperature, it may be possible for Sr to be more effectively removed from the biomineralization site when more energy is available. For the same reason, the bivalve can likely also better control microstructural properties. In contrast, during formation of the annual growth lines, metabolic rates are strongly reduced, and the energy is thus limited. Instead of highly complex microstructures (HOM, CA), the bivalve then forms Sr-rich irregular simple/spherulitic prisms that are similar in habit though smaller than the spherulitic grains observed in inorganic aragonite [61]. If that interpretation is correct, the shell Sr/Ca and BMU size would be merely indirectly correlated with each other.

The incorporation of trace metals into $CaCO_3$ also depends on the crystal habit and varies among the different crystal faces, amongst others, due to crystal lattice defects. For example, in the case of calcite, Sr^{2+} incorporation is facilitated by increased amounts of crystal lattice defects [104,105]. The same applies to the incorporation of Mg^{2+} into aragonite [106]. Due to a different mode of growth [105], some crystal faces (e.g., the dominant {1014} face in calcite) develop more lattice defects than others, which significantly lowers the energetic cost of Mg^{2+} and Sr^{2+} incorporation. Furthermore, the substitution of Ca^{2+} by Mg^{2+}, and especially by Sr^{2+}, is energetically less costly on the surface of aragonite than deeper inside the crystal [107,108]. Therefore, large, exposed crystal faces should promote the incorporation of trace impurities. If different crystal faces provide variable opportunities for trace metal incorporation [105,109], and larger amounts of trace impurities can be accommodated on large, exposed crystal surfaces [107,108], the Sr content of the shell may thus be intimately linked to the BMU habit [55]. Idiomorphic BMUs with well-developed primary crystal faces may thus accommodate a larger number of strontium ions than xenomorphic BMUs, which lack a characteristic habit due to competition with neighboring BMUs during growth. This interpretation would fit well with the observed Sr/Ca differences among the different microstructures. Blocky, idiomorphic BMUs present at annual growth lines possess well-developed crystal faces and, accordingly, show the largest Sr/Ca values (Table S2, [69–71]). Biomineral units of the oOSL (HOM), in contrast, are not idiomorphic in habit and consist of several co-aligned or twinned crystals (i.e., irregularly shaped crystallites). This suggests that the development of ideal crystal growth faces is inhibited during the formation of BMUs of the homogenous microstructure, which is likely the reason why they contain less Sr^{2+} than the irregular simple/spherulitic prisms found at the annual growth lines. The CA-BMUs of the iOSL are highly ramified, convoluted and interfingered, and hence probably possess the least developed primary crystal faces. Accordingly, the iOSL contains less Sr than the oOSL.

Following the hypothesis that Sr^{2+} incorporation into the shell aragonite depends on the degree of idiomorphism of the BMUs, (microstructure-specific) correlations between Sr/Ca and the BMU size should occur (Figure 6a). Sr/Ca values of both sublayers of the

outer shell layer of *A. islandica* decreased with an increasing BMU size, which is expected, given that an increasing size also leads to increased twinning (HOM) and ramification of the BMU outline (CA). In contrast, the large idiomorphic BMUs of the annual growth lines have larger, well-developed crystal faces and, thus, contain more Sr.

If Sr/Ca is indeed coupled to the shell microstructure via preferential incorporation along specific crystal faces, then this coupling could be better described and predicted by the surface area-to-volume (SA/Vol) ratio of the BMUs rather than by the BMU area. Large SA/Vol ratios indicate highly convoluted BMU contours, and, hence, less Sr^{2+}-accommodating crystal surfaces. Unfortunately, it is not yet possible to image individual sub-μm-sized BMUs in three dimensions, so the SA/Vol ratios of the BMUs cannot currently be directly measured. However, SA/Vol ratios increase in smaller and less rounded objects. Accordingly, the small, equidimensional HOM-BMUs (Figure 1f) likely come with a lower SA/Vol ratio than the slightly larger, more acute and ramified CA-BMUs (Figure 1f). If this hypothetical correlation between SA/Vol ratios and BMU size actually exists, the microstructure-dependent seasonal variation in Sr/Ca could be related to changing SA/Vol ratios. Element incorporation into shells may generally be affected by changing BMU SA/Vol ratios because they regulate the exchange rates of ions, heat, energy and many other physical properties [110,111]. Thus, SA/Vol ratios could be used as a proxy to explain the preferential incorporation of Sr into the HOM microstructure of the oOSL. If three-dimensional SA/Vol data were available, a more robust relationship could likely be identified between the shell Sr/Ca and microstructure.

Organic components likely also play a major role during microstructure formation and Sr^{2+} incorporation. Organic matrices promote crystal nucleation and spatially confine the BMUs during formation [112–114], which ultimately not only determines the overall microstructure type but also the mechanical properties of the bioceramic (cf. [103]). Organic matrices can likely also promote or inhibit the incorporation of trace impurities into the crystal lattice by controlling the development of cation-affine crystal surfaces or by causing lattice defects. For example, in abiogenic precipitation experiments, the addition of shell-associated organic components promoted the incorporation of Mg^{2+} into the calcite crystal lattice [71,115]. A similar mechanism may explain the incorporation of Sr^{2+} into aragonite, because higher Sr/Ca values are typically found in organic-rich shell portions [93,96,97,116], and specifically those dominated by sulfur [71,117,118]. Accordingly, the S/Ca and Sr/Ca of bivalve shells typically co-vary with each other [68,71].

However, strontium and sulfur (and thus organics) are not only much higher within, but also somewhat elevated near (=at both side of) the annual growth lines [68,71], i.e., in shell portions dominated by the largest and smallest BMUs, respectively. Whereas higher levels of Sr in the ISP-BMUs can be explained by strongly reduced vital effects during formation of the growth lines, the elevated Sr concentration in shell portions with smaller BMUs may be explained by organic-bound Sr. In fact, instead of substituting for calcium in the crystal lattice, strontium can also be covalently bound to sulfur-rich organic macromolecules [71,118]. The higher organic content of the portions in the immediate adjacency of the annual growth lines may result from a large SA/Vol ratio of the small HOM and CA-BMUs.

The link between shell organics and strontium content—whether Sr^{2+} is accommodated in the crystal lattice and/or bound to organics—can also help in the understanding of why the amount of this metal is overall higher in the oOSL than in the iOSL. The former contains more organic components than the latter, which is indicated, for example, by higher pigment concentrations in the oOSL [119], as well as higher S/Ca values [71]. Similar findings have been reported from other bivalves species; e.g., in *Ruditapes philippinarum*, the oOSL is enriched in sulfur and Mg [120]. If the BMU size (within the same microstructure type) is negatively correlated to the shell organic content (larger SA/Vol ratio = more organics in smaller BMUs), the BMU area can serve as a surrogate to assess microstructure or organic compound-dependent variations in shell Sr/Ca until high-resolution analyses of shell organics are available.

In conclusion, the data of this study revealed a link between the BMU size and shell Sr/Ca values. This correlation partly explained the Sr partitioning between the biomineralization fluid (extrapallial fluid) and the two sublayers of the outer shell layer (oOSL, iOSL) of *A. islandica*, as well as the intra-annual Sr/Ca variability. However, other properties may be more suitable for explaining the coupling between the shell microstructure and Sr/Ca, because a microstructure-specific Sr enrichment would not be expected if a direct link existed between the BMU size and Sr/Ca. As Sr^{2+} may be preferentially incorporated into aragonite along specific crystal faces, and organics not only control the microstructure formation but can also bind strontium, both the BMU SA/Vol ratios as well as the amount and composition of organic components likely affect shell Sr/Ca values. Until three-dimensional analyses of BMUs are possible and a detailed, high-resolution mapping of shell organics is available, the BMU size serves as a mean to assess microstructure-dependent variations in shell Sr/Ca, even if the two parameters are not directly linked to each other.

4.3. The Influence of Shell Growth Rate on Sr/Ca

Sr/Ca ratios of both sublayers of the outer shell layer were weakly and non-linearly linked to the shell growth rate (Figure 6a). However, the signs of the regression slopes differed between the iOSL and oOSL. Sr/Ca_{oOSL} correlated negatively with the shell growth rate, whereas the opposite was observed in the iOSL. Furthermore, Sr/Ca_{hinge} values compared well with Sr/Ca_{iOSL} data, irrespective of the drastically different growth rates of the two shell portions (Figure 1b). These findings may suggest that no direct relationship exists between Sr/Ca_{shell} and the shell growth rate, or that other factors had a larger impact.

Inconsistent results on the relationship between the growth rate and Sr/Ca in shell aragonite have also been reported from many other bivalve species. While some authors noticed positive correlations (*Spisula solidissima*: [89]; *Leukoma staminea*: [121]; *Saxidomus gigantea*: [90]), others observed inverse relationships between Sr/Ca and the growth rate (inner shell layer of *Mytilus edulis*: [52]). Opposing findings also came from the same species. For example, in *Mercenaria mercenaria*, ref. [89] identified a positive correlation, but according to [90], no relationship exists at all between Sr/Ca and the shell growth rate in this species. In *A. islandica*, similar discrepant findings were made. Whereas [55,59] did not find any significant correlation between Sr/Ca and the shell growth rate in juvenile, lab-grown and some decades-old field-grown *A. islandica* specimens, respectively, ref. [56] identified a negative correlation in the hinge of old-grown (several centuries-old) ocean quahogs collected in the field. These results either suggest that no clear relationship exists between the shell growth rate and Sr/Ca, that the relationship is species-specific or that Sr/Ca is actually coupled to bivalve physiology or metabolism and only correlates mathematically but not causally with the growth rate. In cases where opposite findings were made in the same species, ref. [90] discussed the possibility of habitat-specific differences; specifically, the substrate type.

It is worth noting that controversial findings regarding precipitation rate (=kinetic) effects on the partitioning of Sr between the calcifying fluid and the mineral also came from inorganically precipitated aragonite and theoretical considerations for biomineralized tissues. For example, while Sr/Ca ratios increased non-linearly with the precipitation rate in experiments conducted by [61], ref. [122] found no effect of the precipitation rate on Sr/Ca in inorganic aragonite. Perhaps other experimental parameters had a stronger impact on Sr partitioning than kinetic effects. For coral aragonite, ref. [123] expected a negative correlation because a higher precipitation rate is coupled with an increase in active transmembrane Ca^{2+} transport, which would dilute the Sr^{2+} content in the calcifying fluid. In contrast, ref. [124] argued that, during faster growth, an increased ATP-mediated transmembrane Ca^{2+} transport across specialized channels would also result in larger amounts of strontium in the extrapallial fluid of bivalves. This is because strontium can

diffuse more easily through these calcium channels if the calcium gradient between both sites of the membrane is higher.

While differing environmental regimes could explain differences between species or conspecific specimens from different habitats, it remains difficult to understand why growth-rate-related kinetics should differently affect the Sr^{2+} incorporation into shell portions with a different microstructure that formed from the exact same calcifying fluid, namely the oOSL and iOSL (Figure 1b). Is the answer again linked to differences in the BMU habit and the preferential substitution of Ca^{2+} along certain crystal faces—cf. [55]? Is it possible that the incorporation of strontium occurs at a different pace along the different crystal faces that are exposed in the respective microstructures of the oOSL and iOSL? More research is certainly needed to shed light on these aspects.

In summary, both Sr/Ca_{oOSL} and Sr/Ca_{iOSL} were weakly correlated to the shell growth rate, albeit the former negatively and the latter positively. The mechanisms causing these different relationships remain currently unclear and require a better understanding of biomineralization processes.

5. Conclusions

According to the findings of the present study, shell Sr/Ca values of *A. islandica* measured between annual growth lines cannot currently be used to reconstruct water temperature. Shell Sr/Ca data were positively correlated to seawater temperature, even when the apparent correlations with the microstructural properties (BMU area) and growth rate (increment width) were mathematically eliminated. This contradicts thermodynamic predictions and results from inorganic aragonite. It cannot be precluded that temperature is still recorded by shell Sr/Ca, but, if so, the signal is superimposed beyond recognition by other, hitherto unknown environmental forcings. Unless these environmental variables are identified, it will remain impossible to infer seasonal temperature changes from shell Sr/Ca values of the studied species. The general agreement between the seasonal shell Sr/Ca chronologies of contemporaneous specimens indicates that a common environment forcing is at work, which should be understood as encouragement toward the identification of this environmental variable in future studies. Given the strong coupling between Sr/Ca and the biomineral unit size, a detailed characterization of the shell microstructure will most likely remain an integral part of subsequent attempts to reconstruct temperature from shell Sr/Ca. Aside from the BMU area, it may be useful to quantify other BMU parameters, such as the shape and habit in two and three dimensions, and to assess relationships with shell Sr/Ca. In addition, an ultra-high-resolution characterization and mapping of shell organics may help to better understand the Sr distribution patterns in the shells.

Appendix A

Table A1. Overview of the abbreviations used in the paper.

Sclerochronology	
vm	Ventral margin of the shell
OSL	Outer shell layer of the ventral margin of the shell
oOSL	Outer part of the OSL
iOSL	Inner part of the OSL
HOM	Homogenous microstructure, dominating the oOSL
CA	Crossed-acicular microstructure, dominating the iOSL and the hinge
ISP	Irregular simple prismatic microstructure, found at the annual growth lines
BMU	Biomineral unit; microstructures are composed of BMUs and organics
Sr/Ca data	
Sr/Ca_{vm}	Sr/Ca in all of the ventral margin (oOSL and iOSL combined) of the shell
Sr/Ca_{oOSL}	Sr/Ca specifically in the oOSL of the ventral margin of the shell
Sr/Ca_{iOSL}	Sr/Ca specifically in the iOSL of the ventral margin of the shell
Sr/Ca_{hinge}	Sr/Ca in the hinge of the shell
$d_{GR}Sr/Ca_{vm}$	Sr/Ca detrended by a growth rate (GR)-based method for all data from the ventral margin of the shell (colored in magenta or green if the data are for HOM or CA, respectively)
$d_{GR}Sr/Ca_{oOSL}$	Sr/Ca detrended by a growth rate (GR)-based method specifically for oOSL data
$d_{GR}Sr/Ca_{iOSL}$	Sr/Ca detrended by a growth rate (GR)-based method specifically for iOSL data
$d_{MS}Sr/Ca_{vm}$	Sr/Ca detrended by a BMU size (MS)-based method for all data from the ventral margin of the shell (colored in magenta or green if the data are for HOM or CA, respectively)
$d_{MS}Sr/Ca_{oOSL}$	Sr/Ca detrended by a BMU size (MS)-based method specifically for oOSL data
$d_{MS}Sr/Ca_{iOSL}$	Sr/Ca detrended by a BMU size (MS)-based method specifically for iOSL data
$d_{GRMS}Sr/Ca_{vm}$	Sr/Ca detrended by growth rate (GR) and BMU size (MS)-based methods for all data from the ventral margin of the shell (colored in magenta or green if the data are for HOM or CA, respectively)
$d_{GRMS}Sr/Ca_{oOSL}$	Sr/Ca detrended by growth rate (GR) and BMU size (MS)-based methods specifically for oOSL data
$d_{GRMS}Sr/Ca_{iOSL}$	Sr/Ca detrended by growth rate (GR) and BMU size (MS)-based methods specifically for iOSL data
Environmental data set	
SST	Sea surface temperature (°C)

References

1. Ivany, L.C.; Brey, T.; Huber, M.; Buick, D.P.; Schöne, B.R. El Niño in the Eocene greenhouse recorded by fossil bivalves and wood from Antarctica. *Geophys. Res. Lett.* **2011**, *38*, L16709. [CrossRef]
2. Wanamaker, A.D.; Butler, P.G.; Scourse, J.D.; Heinemeier, J.; Eiríksson, J.; Knudsen, K.L.; Richardson, C.A. Surface changes in the North Atlantic meridional overturning circulation during the last millennium. *Nat. Commun.* **2012**, *3*, 899. [CrossRef] [PubMed]
3. Butler, P.G.; Wanamaker, A.D.; Scourse, J.D.; Richardson, C.A.; Reynolds, D.J. Variability of marine climate on the North Icelandic Shelf in a 1357-year proxy archive based on growth increments in the bivalve *Arctica islandica*. *Palaeogeogr. Palaeoclimatol. Palaeoecol.* **2013**, *373*, 141–151. [CrossRef]
4. Lohmann, G.; Schöne, B.R. Climate signatures on decadal to interdecadal time scales as obtained from mollusk shells (*Arctica islandica*) from Iceland. *Palaeogeogr. Palaeoclimatol. Palaeoecol.* **2013**, *373*, 152–162. [CrossRef]
5. Black, B.A.; Dunham, J.B.; Blundon, B.W.; Brim-Box, J.; Tepley, A.J. Long-term growth-increment chronologies reveal diverse influences of climate forcing on freshwater and forest biota in the Pacific Northwest. *Glob. Chang. Biol.* **2015**, *21*, 594–604. [CrossRef]
6. Black, B.A.; Griffin, D.; van der Sleen, P.; Wanamaker, A.D.; Speer, J.H.; Frank, D.C.; Stahle, D.W.; Pederson, N.; Copenheaver, C.A.; Trouet, V.; et al. The value of crossdating to retain high-frequency variability, climate signals, and extreme events in environmental proxies. *Glob. Chang. Biol.* **2016**, *22*, 2582–2595. [CrossRef]
7. Walliser, E.O.; Mertz-Kraus, R.; Schöne, B.R. The giant inoceramid *Platyceramus platinus* as a high-resolution paleoclimate archive for the Late Cretaceous of the Western Interior Seaway. *Cretac. Res.* **2018**, *86*, 73–90. [CrossRef]
8. Jones, D.S. Annual cycle of shell growth increment formation in two continental shelf bivalves and its paleoecologic significance. *Paleobiol.* **1980**, *6*, 331–340. [CrossRef]
9. Trutschler, K.; Samtleben, C. Shell growth of *Astarte elliptica* (Bivalvia) from Kiel Bay (Western Baltic Sea). *Mar. Ecol. Prog. Ser.* **1988**, *42*, 155–162. [CrossRef]
10. Fritz, L.W.; Haven, D.S. Hard clam, *Mercenaria mercenaria*: Shell growth patterns in Chesapeake Bay. *Fish. Bull.* **1983**, *81*, 697–708.
11. Chauvaud, L.; Thouzeau, G.; Paulet, Y.-M. Effects of environmental factors on the daily growth rate of *Pecten maximus* juveniles in the Bay of Brest (France). *J. Exp. Mar. Biol. Ecol.* **1998**, *227*, 83–111. [CrossRef]
12. Clark, G.R. Daily growth lines in some living Pectens (Mollusca: Bivalvia), and some applications in a fossil relative: Time and tide will tell. *Palaeogeogr. Palaeoclimatol. Palaeoecol.* **2005**, *228*, 26–42. [CrossRef]
13. Evans, J.W. Tidal growth increments in the cockle *Clinocardium nuttalli*. *Science* **1972**, *176*, 416–417. [CrossRef] [PubMed]
14. Ohno, T. Palaeotidal characteristics determined by micro-growth patterns in bivalves. *Palaeont.* **1989**, *32*, 237–263.
15. Hallmann, N.; Burchell, M.; Schöne, B.R.; Irvine, G.V.; Maxwell, D. High-resolution sclerochronological analysis of the bivalve mollusk *Saxidomus gigantea* from Alaska and British Columbia: Techniques for revealing environmental archives and archaeological seasonality. *J. Archaeol. Sci.* **2009**, *36*, 2353–2364. [CrossRef]
16. Thébault, J.; Chauvaud, L.; L'Helguen, S.; Clavier, J.; Barats, A.; Jacquet, S.; Pécheyran, C.; Amouroux, D. Barium and molybdenum records in bivalve shells: Geochemical proxies for phytoplankton dynamics in coastal environments? *Limnol. Oceanogr.* **2009**, *54*, 1002–1014. [CrossRef]
17. Hatch, M.B.A.; Schellenberg, S.A.; Carter, M.L. Ba/Ca variations in the modern intertidal bean clam *Donax gouldii*: An upwelling proxy? *Palaeogeogr. Palaeoclimatol. Palaeoecol.* **2013**, *373*, 98–107. [CrossRef]
18. Yamanashi, J.; Takayanagi, H.; Isaji, A.; Asami, R.; Iryu, Y. Carbon and oxygen isotope records from *Tridacna derasa* shells: Toward establishing a reliable proxy for sea surface environments. *PLoS ONE* **2016**, *11*, e0157659. [CrossRef]
19. Kodama, S.; Takayanagi, H.; Yoshii, K.; Nhu Ha, T.T.; Asami, R.; Abe, O.; Iryu, Y. Carbon and oxygen isotope records of *Tridacna squamosa* shells from two different latitudes in the Ryukyu Islands. *Paleontol. Res.* **2021**, *25*, 79–92. [CrossRef]
20. Shaul, W.; Goodwin, L. Geodock (*Panope generosa*: Bivalvia) age as determined by internal growth lines in the shell. *Can. J. Fish. Aquat. Sci.* **1982**, *39*, 632–636. [CrossRef]
21. Buick, D.P.; Ivany, L.C. 100 years in the dark: Extreme longevity of Eocene bivalves from Antarctica. *Geology* **2004**, *32*, 921. [CrossRef]
22. Schöne, B.R.; Fiebig, J.; Pfeiffer, M.; Gleβ, R.; Hickson, J.; Johnson, A.L.A.; Dreyer, W.; Oschmann, W. Climate records from a bivalved Methuselah (*Arctica islandica*, Mollusca; Iceland). *Palaeogeogr. Palaeoclimatol. Palaeoecol.* **2005**, *228*, 130–148. [CrossRef]
23. Wisshak, M.; López Correa, M.; Gofas, S.; Salas, C.; Taviani, M.; Jakobsen, J.; Freiwald, A. Shell architecture, element composition, and stable isotope signature of the giant deep-sea oyster *Neopycnodonte zibrowii* sp. n. from the NE Atlantic. *Deep Sea Res. Part I Oceanogr. Res. Pap.* **2009**, *56*, 374–407. [CrossRef]
24. Selin, N.I.; Dulenina, P.A. The growth and lifespan of the mussel *Crenomytilus grayanus* (Bivalvia: Mytilidae) in the Tatar Strait (Sea of Japan) in connection with the conditions of life at the northern border of the species range. *Russ. J. Mar. Biol.* **2012**, *38*, 318–324. [CrossRef]
25. Moss, D.K.; Ivany, L.C.; Silver, R.B.; Schue, J.; Artruc, E.G. High-latitude settings promote extreme longevity in fossil marine bivalves. *Paleobiology* **2017**, *43*, 365–382. [CrossRef]
26. Schöne, B.R.; Flessa, K.W.; Dettman, D.L.; Goodwin, D.H. Upstream dams and downstream clams: Growth rates of bivalve mollusks unveil impact of river management on estuarine ecosystems (Colorado River Delta, Mexico). *Estuar. Coast. Shelf Sci.* **2003**, *58*, 715–726. [CrossRef]

27. Strom, A.; Francis, R.C.; Mantua, N.J.; Miles, E.L.; Peterson, D.L. Preserving low-frequency climate signals in growth records of geoduck clams (*Panopea abrupta*). *Palaeogeogr. Palaeoclimatol. Palaeoecol.* **2005**, *228*, 167–178. [CrossRef]

28. Scourse, J.; Richardson, C.; Forsythe, G.; Harris, I.; Heinemeier, J.; Fraser, N.; Briffa, K.; Jones, P. First cross-matched floating chronology from the marine fossil record: Data from growth lines of the long-lived bivalve mollusc *Arctica islandica*. *Holocene* **2006**, *16*, 967–974. [CrossRef]

29. Black, B.A.; Copenheaver, C.A.; Frank, D.C.; Stuckey, M.J.; Kormanyos, R.E. Multi-proxy reconstructions of northeastern Pacific sea surface temperature data from trees and Pacific geoduck. *Palaeogeogr. Palaeoclimatol. Palaeoecol.* **2009**, *278*, 40–47. [CrossRef]

30. Butler, P.G.; Richardson, C.A.; Scourse, J.D.; Wanamaker, A.D.; Shammon, T.M.; Bennell, J.D. Marine climate in the Irish Sea: Analysis of a 489-year marine master chronology derived from growth increments in the shell of the clam *Arctica islandica*. *Quat. Sci. Rev.* **2010**, *29*, 1614–1632. [CrossRef]

31. Reynolds, D.J.; Scourse, J.D.; Halloran, P.R.; Nederbragt, A.J.; Wanamaker, A.D.; Butler, P.G.; Richardson, C.A.; Heinemeier, J.; Eiríksson, J.; Knudsen, K.L.; et al. Annually resolved North Atlantic marine climate over the last millennium. *Nat. Commun.* **2016**, *7*, 13502. [CrossRef] [PubMed]

32. Mette, M.J.; Wanamaker, A.D.; Retelle, M.J.; Carroll, M.L.; Andersson, C.; Ambrose, W.G. Persistent multidecadal variability since the 15th century in the Southern Barents Sea derived from annually resolved shell-based records. *J. Geophys. Res. Oceans* **2021**, *126*, e2020JC017074. [CrossRef]

33. Holland, H.A.; Schöne, B.R.; Marali, S.; Jochum, K.P. History of bioavailable lead and iron in the Greater North Sea and Iceland during the last millennium—A bivalve sclerochronological reconstruction. *Mar. Pollut. Bull.* **2014**, *87*, 104–116. [CrossRef]

34. Black, B.A.; Andersson, C.; Butler, P.G.; Carroll, M.L.; DeLong, K.L.; Reynolds, D.J.; Schöne, B.R.; Scourse, J.; van der Sleen, P.; Wanamaker, A.D.; et al. The revolution of crossdating in marine palaeoecology and palaeoclimatology. *Biol. Lett.* **2019**, *15*, 20180665. [CrossRef] [PubMed]

35. Peharda, M.; Schöne, B.R.; Black, B.A.; Corrège, T. Advances of sclerochronology research in the last decade. *Palaeogeogr. Palaeoclimatol. Palaeoecol.* **2021**, *570*, 110371. [CrossRef]

36. Grossman, E.L.; Ku, T.-L. Oxygen and carbon isotope fractionation in biogenic aragonite: Temperature effects. *Chem. Geol.* **1986**, *59*, 59–74. [CrossRef]

37. Wefer, G.; Berger, W.H. Isotope paleontology: Growth and composition of extant calcareous species. *Mar. Geol.* **1991**, *100*, 207–248. [CrossRef]

38. Epstein, S.; Buchsbaum, R.; Lowenstam, H.A.; Urey, H.C. Revised carbonate-water isotopic temperature scale. *Geol. Soc. Am. Bull.* **1953**, *64*, 1315. [CrossRef]

39. Mook, W.G.; Vogel, J.C. Isotopic equilibrium between shells and their environment. *Science* **1968**, *159*, 874–875. [CrossRef]

40. Killingley, J.S.; Berger, W.H. Stable isotopes in a mollusk shell: Detection of upwelling events. *Science* **1979**, *205*, 186–188. [CrossRef]

41. Witbaard, R.; Jenness, M.I.; Van Der Borg, K.; Ganssen, G. Verification of annual growth increments in *Arctica islandica* L. from the North Sea by means of oxygen and carbon isotopes. *Neth. J. Sea Res.* **1994**, *33*, 91–101. [CrossRef]

42. Ansell, A.D. The rate of growth of the hard clam *Mercenaria mercenaria*(L) throughout the geographical range. *ICES J. Mar. Sci.* **1968**, *31*, 364–409. [CrossRef]

43. Kennish, M.J.; Olsson, R.K. Effects of thermal discharges on the microstructural growth of *Mercenaria mercenaria*. *Environ. Geol.* **1975**, *1*, 41–64. [CrossRef]

44. Goodwin, D.H.; Flessa, K.W.; Schöne, B.R.; Dettman, D.L. Cross-calibration of daily growth increments, stable isotope variation, and temperature in the Gulf of California bivalve mollusk *Chione cortezi*: Implications for paleoenvironmental analysis. *Palaios* **2001**, *16*, 387–398. [CrossRef]

45. Witbaard, R.; Duineveld, G.C.A.; Bergman, M. The effect of tidal resuspension on benthic food quality in the southern North Sea. *Senckenberg. Marit.* **2001**, *31*, 225–234. [CrossRef]

46. Eagle, R.A.; Eiler, J.M.; Tripati, A.K.; Ries, J.B.; Freitas, P.S.; Hiebenthal, C.; Wanamaker, A.D.; Taviani, M.; Elliot, M.; Marenssi, S.; et al. The influence of temperature and seawater carbonate saturation state on ^{13}C–^{18}O bond ordering in bivalve mollusks. *Biogeosciences* **2013**, *10*, 4591–4606. [CrossRef]

47. Henkes, G.A.; Passey, B.H.; Wanamaker, A.D.; Grossman, E.L.; Ambrose, W.G.; Carroll, M.L. Carbonate clumped isotope compositions of modern marine mollusk and brachiopod shells. *Geochim. Cosmochim. Acta* **2013**, *106*, 307–325. [CrossRef]

48. Wacker, U.; Fiebig, J.; Tödter, J.; Schöne, B.R.; Bahr, A.; Friedrich, O.; Tütken, T.; Gischler, E.; Joachimski, M.M. Empirical calibration of the clumped isotope paleothermometer using calcites of various origins. *Geochim. Cosmochim. Acta* **2014**, *141*, 127–144. [CrossRef]

49. Fiebig, J.; Bajnai, D.; Löffler, N.; Methner, K.; Krsnik, E.; Mulch, A.; Hofmann, S. Combined high-precision Δ_{48} and Δ_{47} analysis of carbonates. *Chem. Geol.* **2019**, *522*, 186–191. [CrossRef]

50. Nürnberg, D.; Bijma, J.; Hemleben, C. Assessing the reliability of magnesium in foraminiferal calcite as a proxy for water mass temperatures. *Geochim. Cosmochim. Acta* **1996**, *60*, 803–814. [CrossRef]

51. Corrège, T. Sea surface temperature and salinity reconstruction from coral geochemical tracers. *Palaeogeogr. Palaeoclimatol. Palaeoecol.* **2006**, *232*, 408–428. [CrossRef]

52. Dodd, J.R. Environmental control of strontium and magnesium in *Mytilus*. *Geochim. Cosmochim. Acta* **1965**, *29*, 385–398. [CrossRef]

53. Lorrain, A.; Gillikin, D.P.; Paulet, Y.-M.; Chauvaud, L.; Mercier, A.L.; Navez, J.; André, L. Strong kinetic effects on Sr/Ca ratios in the calcitic bivalve *Pecten maximus*. *Geology* **2005**, *33*, 965–968. [CrossRef]

54. Surge, D.; Walker, K.J. Geochemical variation in microstructural shell layers of the southern quahog (*Mercenaria campechiensis*): Implications for reconstructing seasonality. *Palaeogeogr. Palaeoclimatol. Palaeoecol.* **2006**, *237*, 182–190. [CrossRef]

55. Foster, L.C.; Allison, N.; Finch, A.A.; Andersson, C. Strontium distribution in the shell of the aragonite bivalve *Arctica islandica*: Sr in the shell of *Arctica islandica*. *Geochem. Geophys. Geosyst.* **2009**, *10*, Q03003. [CrossRef]

56. Schöne, B.R.; Zhang, Z.; Radermacher, P.; Thébault, J.; Jacob, D.E.; Nunn, E.V.; Maurer, A.-F. Sr/Ca and Mg/Ca ratios of ontogenetically old, long-lived bivalve shells (*Arctica islandica*) and their function as paleotemperature proxies. *Palaeogeogr. Palaeoclimatol. Palaeoecol.* **2011**, *302*, 52–64. [CrossRef]

57. Sano, Y.; Kobayashi, S.; Shirai, K.; Takahata, N.; Matsumoto, K.; Watanabe, T.; Sowa, K.; Iwai, K. Past daily light cycle recorded in the strontium/calcium ratios of giant clam shells. *Nat. Commun.* **2012**, *3*, 761. [CrossRef] [PubMed]

58. Vihtakari, M.; Ambrose, W.G.; Renaud, P.E.; Locke, W.L.; Carroll, M.L.; Berge, J.; Clarke, L.J.; Cottier, F.; Hop, H. A key to the past? Element ratios as environmental proxies in two Arctic bivalves. *Palaeogeogr. Palaeoclimatol. Palaeoecol.* **2016**, *465*, 316–332. [CrossRef]

59. Wanamaker, A.D.; Gillikin, D.P. Strontium, magnesium, and barium incorporation in aragonitic shells of juvenile *Arctica islandica*: Insights from temperature controlled experiments. *Chem. Geol.* **2019**, *526*, 117–129. [CrossRef]

60. Izumida, H.; Yoshimura, T.; Suzuki, A.; Nakashima, R.; Ishimura, T.; Yasuhara, M.; Inamura, A.; Shikazono, N.; Kawahata, H. Biological and water chemistry controls on Sr/Ca, Ba/Ca, Mg/Ca and δ^{18}O profiles in freshwater pearl mussel *Hyriopsis* sp. *Palaeogeogr. Palaeoclimatol. Palaeoecol.* **2011**, *309*, 298–308. [CrossRef]

61. Gaetani, G.A.; Cohen, A.L. Element partitioning during precipitation of aragonite from seawater: A framework for understanding paleoproxies. *Geochim. Cosmochim. Acta* **2006**, *70*, 4617–4634. [CrossRef]

62. Yan, H.; Shao, D.; Wang, Y.; Sun, L. High resolution Sr/Ca profile of *Tridacna gigas* from Xisha Islands of South China Sea and its potential application on sea surface temperature reconstruction. *J. Earth Environ.* **2011**, *2*, 381–386.

63. Yan, H.; Shao, D.; Wang, Y.; Sun, L. Sr/Ca profile of long-lived *Tridacna gigas* bivalves from South China Sea: A new high-resolution SST proxy. *Geochim. Cosmochim. Acta* **2013**, *112*, 52–65. [CrossRef]

64. Yan, H.; Shao, D.; Wang, Y.; Sun, L. Sr/Ca differences within and among three *Tridacnidae* species from the South China Sea: Implication for paleoclimate reconstruction. *Chem. Geol.* **2014**, *390*, 22–31. [CrossRef]

65. Füllenbach, C.S.; Schöne, B.R.; Mertz-Kraus, R. Strontium/lithium ratio in aragonitic shells of *Cerastoderma edule* (Bivalvia)—A new potential temperature proxy for brackish environments. *Chem. Geol.* **2015**, *417*, 341–355. [CrossRef]

66. Zhao, L.; Schöne, B.R.; Mertz-Kraus, R. Controls on strontium and barium incorporation into freshwater bivalve shells (*Corbicula fluminea*). *Palaeogeogr. Palaeoclimatol. Palaeoecol.* **2017**, *465*, 386–394. [CrossRef]

67. Shirai, K.; Takahata, N.; Yamamoto, H.; Omata, T.; Sasaki, T.; Sano, Y. Novel analytical approach to bivalve shell biogeochemistry: A case study of hydrothermal mussel shell. *Geochem. J.* **2008**, *42*, 413–420. [CrossRef]

68. Füllenbach, C.S.; Schöne, B.R.; Shirai, K.; Takahata, N.; Ishida, A.; Sano, Y. Minute co-variations of Sr/Ca ratios and microstructures in the aragonitic shell of *Cerastoderma edule* (Bivalvia)—Are geochemical variations at the ultra-scale masking potential environmental signals? *Geochim. Cosmochim. Acta* **2017**, *205*, 256–271. [CrossRef]

69. Roger, L.M.; George, A.D.; Shaw, J.; Hart, R.D.; Roberts, M.; Becker, T.; McDonald, B.J.; Evans, N.J. Geochemical and microstructural characterisation of two species of cool-water bivalves (*Fulvia tenuicostata* and *Soletellina biradiata*) from Western Australia. *Biogeosciences* **2017**, *14*, 1721–1737. [CrossRef]

70. Schöne, B.R.; Radermacher, P.; Zhang, Z.; Jacob, D.E. Crystal fabrics and element impurities (Sr/Ca, Mg/Ca, and Ba/Ca) in shells of *Arctica islandica*—Implications for paleoclimate reconstructions. *Palaeogeogr. Palaeoclimatol. Palaeoecol.* **2013**, *373*, 50–59. [CrossRef]

71. Shirai, K.; Schöne, B.R.; Miyaji, T.; Radarmacher, P.; Krause, R.A.; Tanabe, K. Assessment of the mechanism of elemental incorporation into bivalve shells (*Arctica islandica*) based on elemental distribution at the microstructural scale. *Geochim. Cosmochim. Acta* **2014**, *126*, 307–320. [CrossRef]

72. Höche, N.; Walliser, E.O.; de Winter, N.J.; Witbaard, R.; Schöne, B.R. Temperature-induced microstructural changes in shells of laboratory-grown *Arctica islandica* (Bivalvia). *PLoS ONE* **2021**, *16*, e0247968. [CrossRef] [PubMed]

73. Jochum, K.P.; Nohl, U.; Herwig, K.; Lammel, E.; Stoll, B.; Hofmann, A.W. GeoReM: A new geochemical database for reference materials and isotopic standards. *Geostand. Geoanalyt. Res.* **2005**, *29*, 333–338. [CrossRef]

74. Jochum, K.P.; Weis, U.; Stoll, B.; Kuzmin, D.; Yang, Q.; Raczek, I.; Jacob, D.E.; Stracke, A.; Birbaum, K.; Frick, D.A.; et al. Determination of reference values for NIST SRM 610-617 glasses following ISO guidelines. *Geostand. Geoanal. Res.* **2011**, *35*, 397–429. [CrossRef]

75. Griffin, W.L. GLITTER: Data reduction software for laser ablation ICP-MS. In *Laser Ablation ICP-MS in the Earth Sciences: Current Practices and Outstanding Issues*; Mineralogy Association of Canada: Quebec City, QC, Canada, 2008; pp. 308–311.

76. Jochum, K.P.; Scholz, D.; Stoll, B.; Weis, U.; Wilson, S.A.; Yang, Q.; Schwalb, A.; Börner, N.; Jacob, D.E.; Andreae, M.O. Accurate trace element analysis of speleothems and biogenic calcium carbonates by LA-ICP-MS. *Chem. Geol.* **2012**, *318–319*, 31–44. [CrossRef]

77. Marali, S.; Schöne, B.R.; Mertz-Kraus, R.; Griffin, S.M.; Wanamaker, A.D.; Butler, P.G.; Holland, H.A.; Jochum, K.P. Reproducibility of trace element time-series (Na/Ca, Mg/Ca, Mn/Ca, Sr/Ca, and Ba/Ca) within and between specimens of the bivalve *Arctica islandica*—A LA-ICP-MS line scan study. *Palaeogeogr. Palaeoclimatol. Palaeoecol.* **2017**, *484*, 109–128. [CrossRef]

78. Höche, N.; Walliser, E.O.; Schöne, B.R. Microstructural mapping of *Arctica islandica* shells reveals environmental and physiological controls on biomineral size. *Front. Earth Sci.* **2022**, *9*, 781305. [CrossRef]

79. Berg, S.; Kutra, D.; Kroeger, T.; Straehle, C.N.; Kausler, B.X.; Haubold, C.; Schiegg, M.; Ales, J.; Beier, T.; Rudy, M.; et al. ilastik: Interactive machine learning for (bio)image analysis. *Nat. Methods* **2019**, *16*, 1226–1232. [CrossRef]

80. van der Walt, S.; Schönberger, J.L.; Nunez-Iglesias, J.; Boulogne, F.; Warner, J.D.; Yager, N.; Gouillart, E.; Yu, T. Scikit-image: Image processing in Python. *PeerJ* **2014**, *2*, e453. [CrossRef]

81. Höche, N.; Walliser, E.O.; Schöne, B.R. Data for "Microstructural Mapping of *A. Islandica* Shells Reveals Environmental and Physiological Controls on Biomineral Size" (1.0) [Data set]. *Zenodo* **2021**. [CrossRef]

82. Hanna, E.; Jónsson, T.; Ólafsson, J.; Valdimarsson, H. Icelandic coastal sea surface temperature records constructed: Putting the pulse on air–sea–climate interactions in the Northern North Atlantic. Part I: Comparison with HadISST1 open-ocean surface temperatures and preliminary analysis of long-term patterns and anomalies of SSTs around Iceland. *J. Clim.* **2006**, *19*, 5652–5666. [CrossRef]

83. Schöne, B.R. *Arctica islandica* (Bivalvia): A unique paleoenvironmental archive of the northern North Atlantic Ocean. *Glob. Planet. Change* **2013**, *111*, 199–225. [CrossRef]

84. Kinsman, D.J.J.; Holland, H.D. The co-precipitation of cations with $CaCO_3$—IV. The co-precipitation of Sr^{2+} with aragonite between 16° and 96 °C. *Geochim. Cosmochim. Acta* **1969**, *33*, 1–17. [CrossRef]

85. Gillikin, D.P.; Lorrain, A.; Paulet, Y.-M.; André, L.; Dehairs, F. Synchronous barium peaks in high-resolution profiles of calcite and aragonite marine bivalve shells. *Geo-Mar. Lett.* **2008**, *28*, 351–358. [CrossRef]

86. Dietzel, M.; Gussone, N.; Eisenhauer, A. Co-precipitation of Sr^{2+} and Ba^{2+} with aragonite by membrane diffusion of CO_2 between 10 and 50 °C. *Chem. Geol.* **2004**, *203*, 139–151. [CrossRef]

87. Hart, S.R.; Blusztajn, J. Clams as recorders of ocean ridge volcanism and hydrothermal vent field activity. *Science* **1998**, *280*, 883–886. [CrossRef] [PubMed]

88. Toland, H.; Perkins, B.; Pearce, N.; Keenan, F.; Leng, M.J. A study of sclerochronology by laser ablation ICP-MS. *J. Anal. At. Spectrom.* **2000**, *15*, 1143–1148. [CrossRef]

89. Stecher, H.A.; Krantz, D.E.; Lord, C.J.; Luther, G.W.; Bock, K.W. Profiles of strontium and barium in *Mercenaria mercenaria* and *Spisula solidissima* shells. *Geochim. Cosmochim. Acta* **1996**, *60*, 3445–3456. [CrossRef]

90. Gillikin, D.P.; Lorrain, A.; Navez, J.; Taylor, J.W.; André, L.; Keppens, E.; Baeyens, W.; Dehairs, F. Strong biological controls on Sr/Ca ratios in aragonitic marine bivalve shells: Controls on Sr/Ca ratios. *Geochem. Geophys. Geosyst.* **2005**, *6*, Q05009. [CrossRef]

91. Schleinkofer, N.; Raddatz, J.; Evans, D.; Gerdes, A.; Flögel, S.; Voigt, S.; Büscher, J.V.; Wisshak, M. Compositional variability of Mg/Ca, Sr/Ca, and Na/Ca in the deep-sea bivalve *Acesta excavata* (Fabricius, 1779). *PLoS ONE* **2021**, *16*, e0245605. [CrossRef]

92. Shen, C.-C.; Liu, K.-K.; Lee, M.-Y.; Lee, T.; Wang, C.-H.; Lee, H.-J. A novel method for tracing coastal water masses using Sr/Ca ratios and salinity in Nanwan Bay, southern Taiwan. *Estuar. Coast. Shelf Sci.* **2005**, *65*, 135–142. [CrossRef]

93. Schöne, B.R.; Zhang, Z.; Jacob, D.; Gillikin, D.P.; Tütken, T.; Garbe-Schönberg, D.; McConnaughey, T.; Soldati, A. Effect of organic matrices on the determination of the trace element chemistry (Mg, Sr, Mg/Ca, Sr/Ca) of aragonitic bivalve shells (*Arctica islandica*)—Comparison of ICP-OES and LA-ICP-MS data. *Geochem. J.* **2010**, *44*, 23–37. [CrossRef]

94. Ropes, J.H. Procedures for preparing acetate peels and evidence validating the annual periodicity of growth lines formed in the shells of ocean quahogs, *Arctica islandica*. *Mar. Fish. Rev.* **1984**, *46*, 27–35.

95. Dunca, E.; Mutvei, H.; Göransson, P.; Mörth, C.-M.; Schöne, B.R.; Whitehouse, M.J.; Elfman, M.; Baden, S.P. Using ocean quahog (*Arctica islandica*) shells to reconstruct palaeoenvironment in Öresund, Kattegat and Skagerrak, Sweden. *Int. J. Earth Sci.* **2009**, *98*, 3–17. [CrossRef]

96. Karney, G.B.; Butler, P.G.; Scourse, J.D.; Richardson, C.A.; Lau, K.H.; Czernuszka, J.T.; Grovenor, C.R.M. Identification of growth increments in the shell of the bivalve mollusc *Arctica islandica* using backscattered electron imaging: Identification of growth increments in the shell of the bivalve mollusc. *J. Microsc.* **2011**, *241*, 29–36. [CrossRef]

97. Karney, G.B.; Butler, P.G.; Speller, S.; Scourse, J.D.; Richardson, C.A.; Schröder, M.; Hughes, G.M.; Czernuszka, J.T.; Grovenor, C.R.M. Characterizing the microstructure of *Arctica islandica* shells using NanoSIMS and EBSD. *Geochem. Geophys. Geosyst.* **2012**, *13*, Q04002. [CrossRef]

98. Markulin, K.; Peharda, M.; Mertz-Kraus, R.; Schöne, B.R.; Uvanović, H.; Kovač, Ž.; Janeković, I. Trace and minor element records in aragonitic bivalve shells as environmental proxies. *Chem. Geol.* **2019**, *507*, 120–133. [CrossRef]

99. Goldschmidt, V.M. Die Gesetze der Krystallochemie. *Naturwissenschaften* **1926**, *14*, 477–485. [CrossRef]

100. Amiel, A.J.; Friedman, G.M.; Miller, D.S. Distribution and nature of incorporation of trace elements in modern aragonitic corals. *Sedimentology* **1973**, *20*, 47–64. [CrossRef]

101. Speer, J.A. Chapter 5. Crystal chemistry and phase relations of orthorhombic carbonates. In *Carbonates*; Reeder, R.J., Ed.; De Gruyter: Washington, DC, USA, 1983; pp. 145–190. ISBN 978-1-5015-0813-4.

102. Lebrato, M.; Garbe-Schönberg, D.; Müller, M.N.; Blanco-Ameijeiras, S.; Feely, R.A.; Lorenzoni, L.; Molinero, J.-C.; Bremer, K.; Jones, D.O.B.; Iglesias-Rodriguez, D.; et al. Global variability in seawater Mg:Ca and Sr:Ca ratios in the modern ocean. *Proc. Natl. Acad. Sci. USA* **2020**, *117*, 22281–22292. [CrossRef]

103. Boon, P.J.; Cooksley, S.L.; Geist, J.; Killeen, I.J.; Moorkens, E.A.; Sime, I. Developing a standard approach for monitoring freshwater pearl mussel (*Margaritifera margaritifera*) populations in European rivers. *Aquatic. Conserv. Mar. Freshw. Ecosyst.* **2019**, *29*, 1365–1379. [CrossRef]

104. Plummer, L.N.; Busenberg, E. Thermodynamics of aragonite-strontianite solid solutions: Results from stoichiometric solubility at 25 and 76 °C. *Geochim. Cosmochim. Acta* **1987**, *51*, 1393–1411. [CrossRef]

105. Paquette, J.; Reeder, R.J. Relationship between surface structure, growth mechanism, and trace element incorporation in calcite. *Geochim. Cosmochim. Acta* **1995**, *59*, 735–749. [CrossRef]

106. Mavromatis, V.; Brazier, J.-M.; Goetschl, K.E. Controls of temperature and mineral growth rate on Mg incorporation in aragonite. *Geochim. Cosmochim. Acta* **2022**, *317*, 53–64. [CrossRef]

107. Menadakis, M.; Maroulis, G.; Koutsoukos, P.G. Incorporation of Mg^{2+}, Sr^{2+}, Ba^{2+} and Zn^{2+} into aragonite and comparison with calcite. *J. Math. Chem.* **2008**, *46*, 484–491. [CrossRef]

108. Kawano, J.; Sakuma, H.; Nagai, T. Incorporation of Mg^{2+} in surface Ca^{2+} sites of aragonite: An *ab initio* study. *Prog. Earth Planet. Sci.* **2015**, *2*, 7. [CrossRef]

109. Reeder, R.J.; Grams, J.C. Sector zoning in calcite cement crystals: Implications for trace element distributions in carbonates. *Geochim. Cosmochim. Acta* **1987**, *51*, 187–194. [CrossRef]

110. Glazier, D.S. A unifying explanation for diverse metabolic scaling in animals and plants. *Biol. Rev.* **2010**, *85*, 111–138. [CrossRef]

111. Okie, J.G. General models for the spectra of surface area scaling strategies of cells and organisms: Fractality, geometric dissimilitude, and internalization. *Am. Nat.* **2013**, *181*, 421–439. [CrossRef]

112. Gotliv, B.-A.; Addadi, L.; Weiner, S. Mollusk shell acidic proteins: In search of individual functions. *ChemBioChem* **2003**, *4*, 522–529. [CrossRef]

113. Cusack, M.; Freer, A. Biomineralization: Elemental and organic influence in carbonate systems. *Chem. Rev.* **2008**, *108*, 4433–4454. [CrossRef] [PubMed]

114. Ren, D.; Feng, Q.; Bourrat, X. Effects of additives and templates on calcium carbonate mineralization in vitro. *Micron* **2011**, *42*, 228–245. [CrossRef] [PubMed]

115. Wang, D.; Wallace, A.F.; De Yoreo, J.J.; Dove, P.M. Carboxylated molecules regulate magnesium content of amorphous calcium carbonates during calcification. *Proc. Natl. Acad. Sci. USA* **2009**, *106*, 21511–21516. [CrossRef] [PubMed]

116. Lorens, R.B.; Bender, M.L. The impact of solution chemistry on *Mytilus edulis* calcite and aragonite. *Geochim. Cosmochim. Acta* **1980**, *44*, 1265–1278. [CrossRef]

117. Tanabe, K. Age and growth rate determinations of an intertidal bivalve, *Phacosoma japonicum*, using internal shell increments. *Lethaia* **1988**, *21*, 231–241. [CrossRef]

118. Yoshimura, T.; Tamenori, Y.; Suzuki, A.; Nakashima, R.; Iwasaki, N.; Hasegawa, H.; Kawahata, H. Element profile and chemical environment of sulfur in a giant clam shell: Insights from μ-XRF and X-ray absorption near-edge structure. *Chem. Geol.* **2013**, *352*, 170–175. [CrossRef]

119. Stemmer, K.; Nehrke, G. The distribution of polyenes in the shell of *Arctica islandica* from North Atlantic localities: A confocal Raman microscopy study. *J. Molluscan Stud.* **2014**, *80*, 365–370. [CrossRef]

120. Poulain, C.; Gillikin, D.P.; Thébault, J.; Munaron, J.M.; Bohn, M.; Robert, R.; Paulet, Y.-M.; Lorrain, A. An evaluation of Mg/Ca, Sr/Ca, and Ba/Ca ratios as environmental proxies in aragonite bivalve shells. *Chem. Geol.* **2015**, *396*, 42–50. [CrossRef]

121. Takesue, R.K.; van Geen, A. Mg/Ca, Sr/Ca, and stable isotopes in modern and Holocene *Protothaca staminea* shells from a northern California coastal upwelling region. *Geochim. Cosmochim. Acta* **2004**, *68*, 3845–3861. [CrossRef]

122. Zhong, S.; Mucci, A. Calcite and aragonite precipitation from seawater solutions of various salinities: Precipitation rates and overgrowth compositions. *Chem. Geol.* **1989**, *78*, 283–299. [CrossRef]

123. Sinclair, D.J.; Sherwood, O.A.; Risk, M.J.; Hillaire-Marcel, C.; Tubrett, M.; Sylvester, P.; McCulloch, M.; Kinsley, L. Testing the reproducibility of Mg/Ca profiles in the deep-water coral *Primnoa resedaeformis*: Putting the proxy through its paces. In *Cold-Water Corals and Ecosystems*; Freiwald, A., Roberts, J.M., Eds.; Erlangen Earth Conference Series; Springer: Berlin/Heidelberg, Germany, 2005; pp. 1039–1060. ISBN 978-3-540-24136-2.

124. Carré, M.; Bentaleb, I.; Bruguier, O.; Ordinola, E.; Barrett, N.T.; Fontugne, M. Calcification rate influence on trace element concentrations in aragonitic bivalve shells: Evidences and mechanisms. *Geochim. Cosmochim. Acta* **2006**, *70*, 4906–4920. [CrossRef]